Scientific Reports

https://doi.org/10.1038/s41598-026-40288-x

Article in Press

Waste *citrus pseudolimon* peels derived biochar assisted magnetic Zn + Al (LDH) nanocomposites for As (III) adsorption

Received: 7 August 2025

Accepted: 11 February 2026

Published online: 25 March 2026

Cite this article as: Sharma S., Sharma N., Somvanshi A. *et al.* Waste *citrus pseudolimon* peels derived biochar assisted magnetic Zn + Al (LDH) nanocomposites for As (III) adsorption. *Sci Rep* (2026). https://doi.org/10.1038/s41598-026-40288-x

Suchi Sharma, Nadeem Sharma, Anand Somvanshi, Abdulrhman Alsayari, Shadma Wahab, Ajay Kumar, Deepak Pathania, Abhishek Thakur, Rohit Jasrotia, Arush Sharma & Allah Dekama Jara

Waste *Citrus pseudolimon* peels derived biochar assisted magnetic Zn+Al (LDH) nanocomposites for As (III) adsorption

Suchi Sharma[1,6], Nadeem Sharma[1], Anand Somvanshi[2], Abdulrhman Alsayari[3], Shadma Wahab[3], Ajay Kumar[4], Deepak Pathania[5], Abhishek Thakur[6], Rohit Jasrotia[7,8,9], Arush Sharma[6]*, Allah Dekama Jara[10]*

[1]*Department of Chemistry, Maharishi Markandeshwar Engineering College (MMEC), Maharishi Markandeshwar Deemed to be University (MMDU), Ambala, Haryana (India)-133207*

[2]*Department of Physics (Applied Science), Parul University, Vadodara, Gujarat, 391760, India*

[3]*Department of Pharmacognosy, College of Pharmacy, King Khalid University, Abha, 61421, Saudi Arabia*

[4]*Department of Chemistry, School of Basic and Applied Sciences, Maharaja Agrasen University (MAU), Atal Shiksha Kunj, Solan, (HP), 174103, India*

[5]*Department of Environmental Science, Central University of Jammu, Bagla (Rahya-Suchani), Samba, Jammu and Kashmir, 181143, India.*

[6]*Department of Chemistry, School of Sciences, Baddi University of Emerging Sciences and Technology (BUEST), Solan, (HP) 173205, India*

[7]*School of Physics and Materials Science, Shoolini University, Solan, Himachal Pradesh, 173229, India*

[8]*Department of Physics, Graphic Era University (Deemed to be University), Dehradun, India*

[9]*Centre for Research Impact & Outcome, Chitkara University Institute of Engineering and Technology, Chitkara University, Rajpura, Punjab, 140401, India*

[10]*Adama Science and Technology University, Center of Excellence for Advanced Materials Science and Engineering, department of Materials Science and Engineering, Adama, Ethiopia*

***Corresponding Author's email ids:** allah.dekama@astu.edu.et, arush766@gmail.com

Abstract

Arsenic (III) ion contamination in water system is a significant and challenging global concern. In this study, agro-waste material, specifically *Citrus pseudolimon* peels (CP), was utilized as a precursor for the preparation of biochar (CPB). Furthermore, biochar-supported Fe_3O_4-Zn+Al layered double hydroxide (M-CPB/LDH) has been synthesized by simple co-precipitation method for the removal of noxious As (III) ions. The prepared composites undergone instrumental analysis including Fourier-transform infrared spectroscopy (FTIR), X-ray diffraction (XRD), field-emission scanning electron microscopy (FESEM) equipped with energy-dispersive X-ray spectroscopy (EDX) and elemental mapping, high-resolution transmission electron microscopy (HRTEM), Brunauer-Emmett-Teller (BET), thermo-gravimetric (TGA), vibrating sample magnetometer (VSM), and X-ray photoelectron spectroscopy (XPS). The surface areas (BET) of CPB and M-CPB/LDH composites were recorded to be 52.49 m^2/g and 99.78 m^2/g, respectively. The VSM analysis confirmed the ferromagnetic characteristics of M-CPB/LDH composites. The adsorption behavior of CPB, M-LDH and M-CPB/LDH composites was strongly depend on pH, with the maximum As (III) ion uptake recorded at pH 4.0. The sorption of As (III) ion were analyzed by isotherm, kinetics and thermodynamic study. Experimental data obey the Langmuir model (R^2=0.97-0.99), indicating that As (III) ions exhibits the monolayer adsorption. The kinetic results directed that removal mechanism conformed to pseudo-second-order model, signifying the chemisorption play

a major role. The maximum monolayer capacities of CPB, M-LDH and M-CPB/LDH composites for As (III) ions were recorded to be 575.10 mg/g, 624.34 mg/g and 721.34 mg/g, respectively. The maximum adsorption of 88.95 %, 92.18 %, and 96.76 % were achieved for CPB, M-LDH and M-CPB/LDH composites, respectively, at 65 °C under optimal conditions, indicating a endothermic and thermodynamically favorable. Regeneration study demonstrated that adsorbents were effectively recovered using 0.01 mol/L HCl as the desorbing agent. After seven adsorption-desorption cycles, the adsorption remained at 78.19 %, 83.13 %, and 91.45 % for CPB, M-LDH, and M-CPB/LDH composites, respectively. Finally, we summarize that synthesized M-CPB/LDH composite exhibited high efficiency, versatility and economical for As (III) ion removal, making it a promising material for wastewater treatment.

Keywords: *Citrus pseudolimon* peels, Biochar, Zn+Al (LDH), As (III), Isotherm, Kinetics

1. Introduction

Environmental contamination is among the most pressing global challenges. This problem arises from the release of pollutants from countless sources, such as sewage disposal, industrial, and agricultural activities, which introduce harmful metals into the environment [1-2]. Among these contaminants, arsenic (As) is particularly dangerous due to its toxic and cancer-causing properties in aquatic ecosystems. The chronic exposure to extreme arsenic level has caused severe health conditions including diabetes,

cardiovascular and respiratory disorders, neurological functioning and various forms of cancer. As a result, arsenic adulteration is a critical global concern. The permissible limit of 10 µg/L arsenic in intake water has been prescribed by USEPA. However, alarmingly high concentrations up to 5000 mg $L^{\sim 1}$ have been reported in underground water sources, raising concerns among health organizations [3-4].

Various chemical forms of arsenic with differing levels of toxicity are found in nature. As (III) found as $H_2AsO_3^-$, $HAsO_3^{2-}$ and AsO_3^{3-} ions, while As (V) exist as $H_2AsO_4^-$, $HAsO_4^{2-}$ and $AsO_4^{3\cdot}$ The trivalent form of arsenic (As III) being significantly more poisonous than pentavalent (As V) form and As (III) poses a greater health hazard than As (V) [5-6]. Research attention has been centered on developing strategies for speciation of various types of arsenic as well as finding technologies that may remove arsenic contaminated water. Numerous methods have proven effective for remediating As (III) ions and these include membrane-based separation techniques, oxidation-coagulation-precipitation followed by filtering, adsorption, electrocoagulation etc. Adsorption stands out as a popular and effective measure for water detoxification, largely owing to its cost-effectiveness and operational simplicity [7-8]. Adsorbents such as cellulose by-products, hydrogels, resins, and carbon materials have been suggested for the treatment of As(III)-contaminated water. However, many of these materials suffer from drawbacks, including lower adsorption capacity, potential risk of secondary contamination, and difficulties in synthesis [9-10].

Consequently, researchers are focusing on developing novel materials for As (III) remediation. Among these, layered double hydroxides (LDHs) have emerged as a promising option due to their strong anion exchange properties and hydrophilic nature, which enhance their effectiveness [11-13]. LDHs are a class of anionic clays, also known as hydrotalcite-like compounds, with a brucite-like layered structure. Their composition consists of positively charged brucite-like sheets and hydrated interlayer regions containing charge-balancing anions. [14-15]. The $[M^{II}1-x\ M^{III}x\ (OH)_2]^{x+}(A^{n-})x/n\bullet mH_2O$, can be used to describe them. It is also known as [MII-MIII-A], in which trivalent cation M^{+3} such as Al^{3+}, Cr^{3+}, Fe^{3+} and divalent cation (M^{+2}) such as Mg^{2+}, Zn^{2+}, Cu^{2+}, etc. The variable x is defined as the $M^{III}/ (M^{II}+M^{III})$ ratio, m is the number of interlayer water, and A^{n-} indicates exchangeable interlayer anion having negative charge [16-17]. The intercalation mechanisms of layered double hydroxides (LDHs) are a fascinating area of study. Intercalating various anions into the interlayer area via different techniques allows for the significant modification of the LDH's properties. [18-19]. The co-precipitation method is the most widely used for preparing the layered double hydroxides (LDHs) due to its simplicity, affordability, and scalability. This technique efficiently incorporates various metal cations and anions into the composite structure, which can be further enhanced by adding a variety of functional anions, including oxyanions, organic compounds, and physiologically active chemicals, to greatly improve the LDH's characteristics [20]. Numerous studies have found outstanding

pollutant adsorption by Zn-Al layered double hydroxides (LDH) synthesized using co-precipitation technique [21-23]. A drawback of co-precipitation is the production of fine, dispersed particles of LDH. This morphology makes the material difficult to separate and recycle after sorption process, which has in turn hindered the widespread practical use of Zn-Al LDH as an adsorbent. Therefore, finding a solution to this issue is crucial. Magnetic separation is an important technique for enhancing material separation in water, particularly for wastewater treatment. Because of their biocompatibility, reusability, and simplicity of recovery, magnetic adsorbents have been given priority in the water treatment sector [24]. Due to its excellent magnetic responsiveness, low toxicity, and ease of synthesis, magnetite (Fe_3O_4) has been widely used as a magnetic modifier compared to other magnetic materials [25].

Agro-waste-biochar has demonstrated growing attention for wastewater treatment and contaminant removal owing to their porous framework, greater porosity and several functional groups able to interact with a variety of toxic pollutants. Agro-derived biochar is highly economical as it utilizes low-cost agricultural residues that are otherwise considered as waste materials. Its production not only reduces the disposal cost, but also provides a sustainable and affordable material for environmental remediation. In this study, *Citrus pseudolimon* peels (CP) is reported as an effective and eco-friendly adsorbent due to its natural abundance and biodegradable nature. [26-27]. Aforementioned discussion, present research seeks to explore an

efficient adsorbent for removal of As (III) ions by integrating the biochar (CPB) and Fe_3O_4-Zn+Al (LDH) composites. The successful synthesis of composites (M-CPB/LDH) has been confirmed through instrumental analysis and simultaneously, adsorption mechanism including parameter optimization, isotherm, kinetic and temperature study has also carried out in detail.

2. Materials and method

2.1. Chemicals

Chemicals and reagents including zinc nitrate hexahydrate (Zn $(NO_3)_2 \cdot 6H_2O$, ≥98 %), aluminum nitrate nonahydrate (Al $(NO_3)_3 \cdot 9H_2O$, ≥98 %), ferrous chloride tetrahydrate ($FeCl_2 \cdot 4H_2O$, ≥99 %), ferric nitrate dihydrate (Fe $(NO_3)_3 \cdot 2H_2O$, ≥98 %), sodium hydroxide (NaOH, pellets, ≥97 %), ammonia solution ($NH_3 \cdot H_2O$, 25–28% w/w NH_3). sodium arsenite ($NaAsO_2$, ≥98 %) were acquired from Sigma-Aldrich chemicals. Analytical grade (AR) reagents were used, and stock solutions of As (III) ions were prepared in deionized water.

2.2. Preparation of *Citrus pseudolimon* biochar (CPB)

Citrus pseudolimon (CP) peels were obtained from Himachal Pradesh, India. Through the pyrolysis process, biochar was produced from the *Citrus pseudolimon* (CP) feedstock. The surface was treated with double distilled water, sun dried after cutting into small pieces to remove any grit or dust left behind. The dried *Citrus pseudolimon* peels were crushed and screened to a particle size of 10 µm. A particle size of 10 µm was chosen in order to

provide a higher surface area, facilitate efficient heat and mass transfer, and ensure homogeneous pyrolysis of material [28]. It was then put into silica crucible having a controlled heating rate of 10 °C/min at 400 °C in a muffle furnace. The silica crucible was removed from muffle furnace and cooled under ambient conditions. The residues weight was measured for the evaluation of biochar yield. The resulting *Citrus pseudolimon* biochar (CPB) was kept in a hermetic vessel for succeeding experiments.

2.3. Synthesis of M-LDH and M-CPB/LDH composites

The Fe_3O_4 nanoparticles were synthesized by adding 1.63 g of $Fe(NO_3)_3 \cdot 9H_2O$ (0.02 mol/L) in 80 mL of double-distilled water along with a 1M NaOH solution. Then, 0.12 g of $FeCl_2$ was added and mixture was thoroughly stirred. Subsequently, solution pH was adjusted to around 10.0 using 0.1 mol/L ammonia solution. The solution was agitated for 3 h continuously and samples were allowed to stand overnight at room temperature (~25 °C) under ambient atmospheric conditions. The Fe_3O_4 precipitates rinses multiple times using deionized water, collected by external magnet and dried in an oven at 65 °C. The obtained black precipitate was labeled as magnetic Fe_3O_4 nanoparticles (M). The M-LDH was synthesized using co-precipitation process. Firstly, a 100 mL solution was prepared by mixing 50 mL each of $Zn(NO_3)_2$ (0.16 mol/L) and $Al(NO_3)_3$ (0.08 mol/L) in double-distilled water, maintaining a molar ratio of 2:1. The solution was magnetically shaken for 35 min. Next, 1.24 g of the previously prepared Fe_3O_4 nanoparticles were added and the mixture was stirred again for 35 min at 65 °C. The NaOH (1M)

solution added dropwise to maintain a pH of 10.0, followed by stirring for 2 h to ensure proper mixing. The mixture was kept undisturbed for 24 h in an oven at 65 °C. The aged precipitates were subjected to washing several times with deionized water until effluent solution reached a neutral pH, then dried at 65 °C in oven-. The final dark powder was labeled as M-Zn+Al (LDH). M-CPB/LDH composites were synthesized by adding 2.0 g of CPB into 80 mL of M-LDH solution. The mixture was stirred for 3 h to ensure sufficient contact between CPB and M-LDH. It was then set aside for 2 h and precipitates were cleaned with distilled water upto neutral pH was reached and then oven drying at 80 °C. Finally, black product crushed using mortar and pestle, and resulting fine powder (approximate yield=2.9 g) was labeled as M-CPB/LDH. The pictorial representation for preparation of CPB, M-LDH and M-CPB/LDH composites has given in Fig. 1

2.4. Characterization

The synthesized M-CPB/LDH composites has been tested using various instrumental techniques. The microstructure was analyzed using field emission-scanning electron microscopy (FESEM) Model Hitachi-PU 5.0 kV and energy dispersive spectroscopy (EDS), elemental analyzer for CHN (Thermo scientific). Diffraction pattern (XRD) was recorded by the Rigaku Smart Lab SE by powder method using Cu K-aplha -1 radiation. Fourier-transform infrared spectra (FT-IR) were examined by Thermo Nicolet FTIR spectrometer with resolution 1cm^{-1} and scan range of 4000^{-1} to 380^{-1}. Using an instrument made by Micrometrics ASAP 2460, surface area and pore

structure were examined by BET instrument (Brunauer-Emmett-Teller). A vibrating sample magnetometer (VSM) is used to check the magnetization by model Quantum Design Linear Motor Servo Controller. High resolution transmission electron microscopy (HRTEM) direct the internal atomic structure of material by Hitachi (H-7500). X-ray photoelectron spectroscopy (XPS) technique measure the composition, chemical state and bonding by Model PHI 5000 Versa Probe III. Themo-gravimetric analysis (TGA) is used to study the material mass changes with altering the temperature by Model (SII 6300 EXSTAR) with temperature range upto 900 °C. The atomic absorption spectrophotometer (AAS) PerkinElmer's PinAAcle 900 series has recorded the As (III) concentration. Zeta potential of prepared sample is calculated on Zeta Potential Analyzer using Malvern Zetasizer Nano ZS installed in MMEC, Ambala.

2.5. Batch experiment

The batch experiment has been conducted to optimize the various parameters and to ensure boosted adsorption of As (III) ions. The experimental were performed in Erlenmeyer flasks (250 mL) having 100 mL of As (III) solution and shaken at 170 rpm in a thermostatic shaker. The effect of M-CPB/LDH dosage (0.050-0.350 g/L), pH (2.0-12.0), initial As (III) concentration (50-350 mg/L), contact time (15-120 min) and temperature (30-60 °C) were systematically investigated and optimized for maximum sorption of toxic As (III) ions. The 0.1 N NaOH and 0.1 N HCl solution were employed to maintain initial pH of As (III) solution. After adsorption. An 8 mL aliquot of the

suspension was withdrawn from the Erlenmeyer flasks and subjected to magnetic separation. The residual concentration of As (III) ions were computed using an AAS at 198 nm. All adsorption experiments were performed quadruplicate to ensure accuracy, consistency and the mean values were reported. The following mathematical equations were applied to calculate the adsorption capacity (q_e) and removal percentage (R %):

$$q_e = \frac{(C_0 - C_e)\, V}{m} \quad (1)$$

$$R\ \% = \frac{C_0 - C_e}{C_0} \times 100 \quad (2)$$

Where, C_0 and C_e (mg L^{-1}) indicate As (III) ion (initial and equilibrium), V and M is the volume (mL) and composites mass (g), respectively.

3. Results and discussion

3.1. Characterization

3.1.1. FTIR and XRD study

FTIR gives the information regarding molecular structure and compositions of a substance by identifying functional groups within the material. FTIR study of CPB, M-LDH, and M-CPB/LDH are revealed in Fig. 2(a). The absorption signal at 3680 cm^{-1} in the CPB is attributed to non-hydrogen-bonded hydroxyl groups arising from residual mineral phases such as metal hydroxides, rather than structural O–H in the carbon matrix [29]. The C-H bending vibration

at 1397 cm^{-1} corresponds to methyl groups in CPB, while absorption signal at 1027 cm^{-1} is attributed to C-O stretching of cellulose and hemicellulose, a characteristic of bio-based materials [30]. The absorption signal at 960 cm^{-1} and 872 cm^{-1} indicates the carbonate groups in the form of calcite group, reflecting the vibrational modes of carbonate. Additionally, signal at 691 cm^{-1} can be assigned to the out-of-plane bending vibration of C-H bonds, which are commonly observe in aromatic or aliphatic hydrocarbons [31]. For M-LDH, absorption signal at 3556 cm^{-1} corresponds to vibration mode of O-H group. The absorption signals recorded at 1642 cm^{-1} and 1345 cm^{-1} are associated with C=C stretching and asymmetric stretching of C-O bond in CO_3^{2-} ions present in the interlayer matrix of M-LDH [32]. The signal at 1023 cm^{-1}, 822 cm^{-1}, and 634 cm^{-1} are ascribed to C-O stretching and vibrational modes of AlO_6 and Al-OH bonds, respectively. Furthermore, absorption signals at 535 cm^{-1} and 422 cm^{-1} were relate to the vibrational modes of Fe-O bond in Fe_3O_4 and Zn-O bond, respectively [33]. This was apparent from Fig. 2(a) that incorporation of CPB into M-LDH results in only slight shifting of peaks and a new peak found at 963 cm^{-1} likely indorsed to the CPB structure. All these peaks successfully showed the formation of M-CPB/LDH composites.

XRD spectra of CPB, M-LDH, and M-CPB/LDH are presented in Fig. 2(b). XRD patterns were recorded in the 2θ range of 10-80° with a step size of 0.02°, and scan rate of 2°/min [34]. In CPB, there is a sharp peak at 2θ = 29.62º indexed as the (002) plane of carbon structure, which is randomly stacked in

the aromatic sheet. Other peaks occurring around 35.91º, 39.74º, 43.36º, 47.65º, and 48.89º can be related to whewellite [$Ca(C_2O_4)\cdot H_2O$] and calcite ($CaCO_3$) compounds [35]. The appearance of calcite peaks is attributed to the fact that *Citrus pseudolimon* (CP) has calcium oxalate present naturally in its leaves, peels and stems. The diffraction peaks of ZA-LDH, which were observed at 2θ values of 23.45º, 35.32º, 39.75º and 62.15º correspond to the reflection planes (hkl) of (006), (012), (018), and (113), respectively. Other peaks found at 18.11º, 29.89º, 33.36º, 43.89º, 54.35º, and 57.08º are designated to the (111), (220), (311), (400), (422), and (511) planes, respectively, and all these peaks agree well with Fe_3O_4 standard card (JCPDS: 79-0417) [36]. The sharp and strong peaks for the (012) and (113) planes in ZA-LDH and the (311) and (511) planes in Fe_3O_4 indicate the successful synthesis of M-LDH. Upon incorporation of CPB onto M-LDH, the crystal structure of M-LDH was slightly altered having introduction of CPB resulting in increased interlayer spacing (d-spacing). The interlayer spacing, as determined from Bragg's law for the (012) plane, was 8.17 Å for M-LDH and 8.26 Å for M-CPB/LDH composites. This expansion of interlayer distance can be explained by the introduction of CPB, which decreases the electrostatic interaction in the brucite-like sheet of M-LDH. As a result, the interlayer distance expands. It is clear from the results that CPB interacts well with the M-LDH structure. Following Debye–Scherrer equation has been employed to computes the average crystallite size:

$$D = \frac{k\lambda}{\beta \cos \theta} \quad (3)$$

Where, D and λ indicate the average crystallite size and X-ray wavelength, respectively. Bragg angle θ, β is full width at half maximum (FWHM) of peaks of diffraction and k is a constant (0.89). The M-CPB/LDH composites exhibits average crystallite size of 13 nm to 18 nm.

3.1.2. BET, TGA and VSM study

The surface area and BJH plot for pore size distribution (PSD) of CPB and M-CPB/LDH composites were studied by N_2 adsorption/desorption isotherm. The curves shape for CPB and M-CPB/LDH represents type IV (a) isotherms with H3 hysteresis loops as stated by IUPAC classification, indicating the presence of micropores and mesopores within a relative pressure (P/P_0) range from approximately 0.551 to 0.1 [37-38]. BET surface area for CPB and M-CPB/LDH composites was computed to be 52.49 m^2/g and 99.78 m^2/g, respectively (Fig. 3a). The main peak of PSD curve (Fig. 3b) for M-CPB/LDH composites was recorded at 3.98 nm and found to be higher than that of CPB (2.48 nm). Other textural properties such as pore volumes of 0.008 cm^3/g and 0.097 cm^3/g were recorded for CPB and M-CPB/LDH composites, respectively. Hence, greater surface area and pore diameter, M-CPB/LDH composites is more conducive for the internal transfer and adsorption of toxic As (III) ions [39]

Thermo-gravimetric (TG) curves of CPB, M-LDH and M-CPB/LDH composites are presented in the Fig. 3(c). Thermal decomposition of the prepared samples follows a three-step mass loss pattern as observed from TGA curve. The first stage of mass loss, occurring around 125.34 °C, corresponds to the evaporation of adsorbed H_2O molecules and volatile substances. The recorded weight losses is approximately 7.70 % for CPB, 4.52 % for M-LDH and 4.03 % for M-CPB/LDH composites [40-41]. As the furnace temperature increase to stage 2, CPB sample exhibits a mass loss of 7.81 %. It is mainly due to decomposition of organic contents such as cellulose and hemicellulose. In contrast, M-LDH and M-CPB/LDH show lower weight losses of 3 % and 3.10 %, respectively. The weight loss chiefly due to dehydroxylation of brucite-like structure of LDH and decomposition of carbonate anions [42]. In the final stage, from 320 °C to 800 °C, the CPB sample shows a small weight loss of 3.18 % is probably not only the breakdown of carbonate ions but also from residual moisture, partial decarbonation of mineral leftovers, and decomposition of oxygen-containing surface functional groups. For M-LDH and M-CPB/LDH, weight losses are 1.40 % and 1.72 %, respectively, linked to the removal of interlayer anions and decarbonation. The thermal stability of M-HLB/LDH is found to be slightly lower than M-LDH composites. This reduced stability corresponds to incorporation of biochar (CPB) into the M-LDH matrix, which likely to deteriorates the M-O bond. Overall, CPB, M-LDH and M-CPB/LDH composites demonstrate significant stability, a crucial criterion for retaining noxious metal ions on their surface.

Magnetization intensity is an important factor for evaluating magnetic properties and directly influencing their magnetic response. The saturation magnetization (Ms) of M-CPB/LDH composites and M-LDH was measured with an applied field ranging from -10,000 to +10,000 kilo-oersted (KOe). From Fig. 3(d), the observed maximum saturation magnetization (Ms) of M-LDH and M-CPB/LDH composites were recorded as 33.59 and 30.87 emu g^{-1}, respectively. VSM parameters values such as saturation magnetization (Ms), coercivity (Hc) and retentivity (Mr) are given in Table 1. The results suggest that M-LDH and M-CPB/LDH composites exhibits ferromagnetic characteristics with enhanced Ms, Hc and Mr values. The slight reduction in magnetization (Ms) of M-CPB/LDH composites mainly attributed to dilution and shielding effect of non-magnetic CPB matrix, that diminishes overall magnetic response per unit mass [43]. However, M-CPB/LDH composites still possess sufficient magnetization strength to be separate out from solutions mixture and collected using an external magnet. As demonstrating in Fig. 3(d) inset that M-CPB/LDH composites can be easily and efficiently retrieved after adsorption experiment. This magnetic separation method provides a significant advantage over centrifugation and filtration techniques, offering a more efficient tool for separation, recovery and reuse of adsorbent.

3.1.3. XPS analysis

The elemental compositions and interactions of M-LDH and M-CPB/LDH composites were scanned using XPS technique. The XPS survey spectrum of M-LDH, confirming the Al, O, Fe, and Zn elements. The survey spectrum of

the M-CPB/LDH composite exhibits an additional peak for C 1s, alongside the parent elemental composition similar to M-LDH, with significant upshifts and downshifts in the respective binding energies (Supplementary Fig.1). Fig. 4(a) illustrates the deconvoluted Al 2p spectrum, where the peaks for M-LDH appear at 72.54 eV and 75.41 eV. In contrast, for M-CPB/LDH, the first peak shows a slight downshift to 71.85 eV, which is attributed to interactions with the CPB surface, potentially altering the oxidation state. An unusual shift in the second peak is also observed, appearing at 86.48 eV, which may be due to Al adopting a different coordination environment onto biochar surface [44-46].

Fig. 4(b) presents the deconvoluted Fe 2p spectrum. In the case of M-LDH, peaks appear at 711.25 eV and 725.16 eV. However, for M-CPB/LDH, both peaks exhibit a downshift, appearing at 709.18 eV and 721.92 eV, respectively. This shift suggests the partial reduction of Fe^{3+} to Fe^{2+} due to interactions with certain electron-rich moieties present on the biochar surface [47-48]. Furthermore, deconvoluted Zn 2p spectrum is presented in Fig. 4(c). For M-LDH, the peaks appear at 1021.58 eV and 1044.98 eV, while for M-CPB/LDH, they shift downward to 1019.16 eV and 1042.40 eV, respectively. Similar to the Fe 2p spectrum, a downward shift in binding energy is observed in the composite. This shift may be attributed to strong interactions with CPB surface functionalities, potentially affecting the Zn–O and Zn–OH bonds present in M-LDH [49-50]. The O 1s spectrum Fig. 4(d) of M-LDH exhibits two peaks: one at 529.96 eV, attributed to M–O and lattice

oxygen within the M-LDH framework, and another at 531.68 eV, corresponding to surface-adsorbed oxygen. In contrast, M-CPB/LDH displays a single peak at 529.21 eV, indicating that M-CPB/LDH composites framework is predominantly characterized by lattice oxygen [51-52]. The deconvoluted C 1s spectrum of M-CPB/LDH, as shown in the Fig. 4(e), exhibits peak at 282.50 eV, 290.69 eV, and 293.57 eV. The signal appearing at lower binding energy of 282.50 eV is ascribed to carbide-like carbon, which likely forms due to interactions between carbon from CPB and metallic species in the LDH moiety. The peak at 290.69 eV corresponds to CO_3^{2-} species, while high-energy peak at 293.57 eV is identified as a satellite peak, attributed to the delocalized aromatic π-electron system present in biochar [53]. Based on aforementioned analysis, it is briefed that M-LDH interacts significantly with the CPB surface, leading to mutual surface modifications that may improve its efficiency for adsorption mechanism.

3.1.4. FESEM, HRTEM, EDS and elemental mapping study

The FESEM and HRTEM scan the microscopic characteristics of synthesized samples. FESEM images of CPB and M-CPB/LDH composites are presented in the Fig. 5(a-f). As observed in the Fig. 5(a-c), CPB surface exposing the porous texture possessing dense, rough, irregular, and elongated or rod-like morphology [54]. The fractured edges indicate that CPB has undergone thermal decomposition, with the residue being a porous carbon-rich structure. The FE-SEM image of ZA-LDH display the typical thin, stacked

nano-sheets and layered flake-like morphology (Fig. 5d). Fig. 5(e-f) shows the microscopic pictures of M-CPB/LDH composites that exhibits uniform, compact and heterogeneous morphology. The occurrence of different particle size and phases indicates the successful loading of brucite like structure of M-LDH on CPB surface (Fig. 5f). HRTEM study reveal (Fig. 5g-i) that M-LDH particles are dark and irregular shaped clusters, indicating the stacking of M-LDH particles on CPB surface (Fig. 5e). The dark lattice spots are for M-LDH and lighter areas indicates the CPB matrix. This was evident from Fig. 5(h) that M-CPB/LDH composites particles were synthesized in the nano-range of 8-14 nm. The SAED pattern (Fig. 5i) confirms the polycrystalline nature of M-CPB/LDH nano-composites with bright and concentric rings.

Fig. 6(a-b) shows the EDS elemental mapping and FESEM image of M-CPB/LDH nanocomposites, upon which analysis was conducted. The EDS spectra (Fig. 6a) validate the occurrence of Al, Fe, C, O, and Zn in the M-CPB/LDH nanocomposites. To determine their adsorption ability, the EDS spectra of As (III) ions loaded CPB, M-LDH, and M-CPB/LDH have been recorded. Figure. 7(a-c) indicates a new peak for As (III) ions is present on the surface of CPB (Fig. 7a), M-LDH (Fig. 7b) and M-CPB/LDH composites (Fig. 7c), verifying their adsorption potential and the presence of As (III) ions was not only confirmed by the appearance of a new peak but also quantitatively validated by the measured atomic % values (Supplementary Table 1, 2 & 3) [55]. Additionally, FESEM image of M-CPB/LDH composites

(Fig. 7d) also shows extensive surface alterations following loading of As (III) ions, supporting structural changes resulting from the sorption process.

3.2. Adsorption: Parameter optimization, isotherm, kinetic and thermodynamic study

3.2.1. Adsorbent dosage effect

The effectiveness of LDH for removal of As (III) ions is highly dependent on sorbent dosage. Theoretically, increasing the sorbent dose improve the adsorption, primarily due to greater surface area and copious sorption sites. As the dispersion of adsorbent increases, accessibility of active sites increases, facilitating the greater interaction and simultaneously removal of As (III) ions. The adsorbent dosage was checked by varying adsorbent dose from 0.050 to 0.350 g/L and findings were illustrated in the Fig. 8(a), shows sorption efficiency (%) rose steeply with adsorbent dosage up to 0.250 g/100 mL. This enhancement mainly due to greater accessibility of adsorption sites and increased surface area of adsorbent, which dictate the diffusion of As (III) ions into the adsorption sites. However, exceeding the dosage beyond 0.250 g/L, the removal percentage began to decline. This reduction is likely due to various factors such as adsorption entrapment, overlapping of sorption sites and potential aggregate formation, which restrict effective surface area to be available for sorption of As (III) ions. The maximum sorption of 88.96 % has been achieved using M-CPB/LDH composites (Fig. 8a), as these prepared

magnetic composites exhibit a significantly higher surface area, enhancing their adsorption capacity.

3.2.2. Solution pH: adsorption mechanism

The surface properties of an adsorbent are highly dependent on pH of adsorbate solution as well as ionic states. It governs not only surface ionization and behavior of its functional group but also dictates molecular forms and degree of ionization for pollutant molecules. Therefore, it is crucial to inspect the sorption behavior of As (III) ions onto CPB, M-LDH, and M-CPLB/LDH composites under various initial pH conditions (2.0-12.0). Furthermore, determining the zero-point charge (pH_{ZPC}) of the prepared samples is crucial, as it provides insight into the charge characteristics of composites at different pH levels. As the solution pH is below pH_{ZPC}, surface of adsorbent is +ve charge and conversely negatively charged. The pH_{ZPC} values of M-HLB/LDH composites were determined using the pH drift method, yielding value of 6.01, as revealed in Fig. 8(b). At pH 4.0, maximum adsorption of 83.11 %, 86.98 %, and 94.56 %, were recorded for CPB, M-LDH and M-CPB/LDH composites, respectively (Fig. 8c). The dominant mechanisms for As (III) ions sorption involve surface complexation, including outer-sphere complexation and ligand exchange mechanism [56-57]. Under acidic conditions, As (III) ions mainly found as H_3AsO_3 and $H_2AsO_3^-$. The surface of M-CPB/LDH composites remains positively charged at pH < pH_{ZPC} due to protonation of -OH groups, facilitating electrostatic interactions with

$H_2AsO_3^-$ ions and boosting the adsorption efficiency. Additionally, -OH groups on the M-CPB/LDH surface participate in a ligand exchange mechanism, further promoting As (III) sorption. As the pH increases beyond 8.0, adsorption capacity gradually declines to 15.15 %, 21.18 % and 32.07 % using CPB, M-LDH and M-CPB/LDH composites respectively due to repulsion interaction between -ve charged composite and deprotonated As (III) species. Based on these findings, pH 4.0 was selected as the optimal for As (III) sorption and consequent experiments were conducted under this pH.

3.2.3. Initial As (III) concentrations and isotherm mechanism

The concentration of As(III) ions plays a vital role in influencing the equilibrium uptake (q_e) and the residual concentration of adsorbate ions in solution. In current study, adsorption of As (III) ions using CPB, M-LDH, and M-CPB/LDH composites, were evaluated under optimized conditions: an adsorbent dosage of 0.250 g/L, pH 4.0 and 30 °C temperature. The As (III) concentration was examined from 50 to 350 mg/L to assess its impact on adsorption efficiency (Fig. 8d). As showed in Fig. 8(d), percentage sorption of As (III) ions present a declining trend. The removal efficiency for CPB, M-LDH, and M-CPB/LDH composites decreased from 89.78 %, 92.78 %, and 95.78 % to 64.78 %, 71.78 %, and 82.78 %, respectively. Among the tested adsorbents, M-CPB/LDH composites demonstrated highest adsorption efficiency across all concentrations, which can be attributed to its enhanced porosity, as confirmed by BET surface area study. The superior adsorption performance of M-CPB/LDH composites is likely due to its greater number of

accessible active sites and improved mass transfer properties compared to CPB and M-LDH. Although, As (III) percentage removal decreased progressively with higher As (III) concentration, but adsorption capacity (q_e) followed an increasing trend. This is mainly due to the driving force generated by concentration gradient between bulk solution and adsorbent surface. At higher As (III) concentrations, mass transfer resistance between aqueous phase and solid adsorbent is overcome more effectively, allowing a greater number of As (III) ions to be retained per unit mass of adsorbent [58]. Based on these findings, 50 mg/L was selected for further experiments to ensure efficient adsorption.

Langmuir, Freundlich and Tempkin models were applied in order to explore the As (III) adsorption mechanism onto CPB, M-LDH, and M-CPB/LDH composites. Langmuir model explain the homogeneous sorption having all sites are equivalent energetically and have same attraction and affinity for adsorbate molecules. Freundlich model correspond to heterogeneous sorption due to the existence of a variety of adsorption sites. Temkin accounts for indirect interactions of adsorbate-adsorbent system with the variations of sorption energy. The linearized equations are given below:

3.2.3.1. Langmuir equation:

$$\frac{C_e}{q_e} = \frac{1}{k_L Q_m} + \frac{C_e}{Q_m} \quad (4)$$

Maximum monolayer capacity and equilibrium constant correspond to Q_m (mg/g) and k_L (L/mg), respectively. The Q_m and k_L accessed from plot of C_e versus Ce/qe, respectively. The R_L (dimensionless separation factor) is used to evaluate the feasibility and found to be favorable, as R_L is $0<R_L<1$. The following equation compute R_L values [59]:

$$R_L = \frac{1}{1+(k_L C_o)} \quad (5)$$

3.2.3.2. Freundlich equation:

$$\ln q_e = \ln k_f + \frac{1}{n}(\ln C_e) \quad (6)$$

The sorption capacity and adsorption intensity are representing by K_F (L/g) and n constants, respectively and obtained from the plot of $\log q_e$ vs. $\log C_e$.

3.2.3.3. Temkin equation:

$$q_e = B\ln(k_T) + B\ln(C_e) \quad (7)$$

Where, k_T and B indicates the Temkin coefficients to be computed from the graph of q_e vs. $\ln C_e$.

The fitting plots are presented in Fig. 9(a-c). It was evident that the linear fit plot for Freundlich model exhibited poorer linearity compared to the Langmuir and Temkin models. Among these, Langmuir model was seeming to be most appropriate for the adsorption of toxic As (III) ions, as indicated by its higher regression coefficient (R^2) values. As depicted in Table 2, Q_m value for As (III) ions by CPB, M-LDH, and M-CPB/LDH composites has been

found to be 575.10 mg/g, 624.34 mg/g and 721.34 mg/g, respectively. The regression coefficient (R^2) values computed from Langmuir model ranged between 0.97-0.99, indicating a strong correlation. The dimensionless separation factor (R_L) determine that weather adsorption is favorable or not. Hence, according to Table 2 and Fig. 9(d), R_L values for CPB, M-LDH and M-CPB/LDH composites were computed to be less than one, confirming that adsorption process followed the Langmuir model [60]. This suggests that As (III) ion sorption occurs in a favorable manner, forming a monolayer sorption onto sorbent surface. Additionally, Temkin model also provided a good linear fit, with regression coefficient (R^2) values ranging from 0.97 to 0.98. This suggests that physical and chemical adsorption involved in sequestration of As (III) ion.

3.2.4. Contact time and kinetic study

The kinetics of As (III) ion removal using CPB, M-LDH and M-CPB/LDH composites were evaluated under optimized conditions: dosage (0.250 g/L), pH (4.0) and initial concentration of As (III) (50 mg/L), with contact time from 15 to 120 min. The As (III) adsorption with function of time is plotted in Fig. 10(a). It was clear that percentage adsorption of As (III) ions onto CPB, M-LDH and M-CPB/LDH composites increased sharply between 15 and 90 min, after which the adsorption uptake gradually decreased (Fig. 10a). The removal efficiency increased from 32.87 %, 42.6 %, and 56.06 % to 88.82 %, 92.77 % and 95.45 %, respectively, after 90 min of shaking. The initial rapid sorption rate due to abundant availability of porous active sites on external

surface of M-CPB/LDH composites, facilitating the adsorption of toxic As (III) ions. Adsorption process shifted to the internal pores of M-CPB/LDH composites as soon as external surface acquire saturation, requiring a longer diffusion time for further amputation of As (III) ions [61]. Hence, 90 min was set for succeeding experiments, as adsorption occurs at a significantly slower rate beyond 90 min due to constrained supply of active sites and diffusion constraints of As (III) ions into the adsorbent pores.

Time-dependency of adsorption process has important role in determining the efficiency of an adsorbent. To understand the adsorption behavior of noxious As (III) ions, applicability of kinetic models including pseudo-first-order, pseudo-second-order, Elovich and Weber-Morris models has been inspected having their equations are given below [62]:

3.2.4.1. Psuedo-first-order model:

$$\log(q_e - q_t) = \log q_e - \frac{k_1}{2.303}t \quad (8)$$

The values of rate constant (k_1) and equilibrium adsorption capacity (q_e) have been calculated from the plot of $\log(q_e-q_t)$ vs. t, respectively.

3.2.4.2. Psuedo-second-order model:

$$\frac{t}{q_e} = \frac{1}{k_2 q^2_e} + \left(\frac{1}{q_e}\right)t \quad (9)$$

k_2 is second-order constant (g mg^{-1} min^{-1}) and k_2 and q_e (mg/g) were computed from t/q_t vs. t.

3.2.4.3. Elovich Model:

$$q_e = \frac{1}{\beta}\ln(\alpha\beta) + \frac{1}{\beta}\ln(t) \quad (10)$$

Where, adsorption rate and degree of surface coverage correspond to α (mg g^{-1} h^{-2}) and β (g mg^{-1}), respectively.

3.2.4.4. Weber-Morris model:

$$q_t = K_{id}t^{0.5} + C \quad (11)$$

Where, C (mg/g) is the intercept, indicates boundary layer thickness and k_{id} rate constant for intraparticle diffusion. The C and k_{id} values are interpreting from q_t vs. $t^{0.5}$ plot.

The applicability of kinetic models has been assessed using their linear fitting plots (Fig. 10b-d). As evident from Table 3, adsorption kinetics of As (III) ions using CPB, M-LDH, and M-CPB/LDH composites were best described by pseudo-second-order model having higher values of R^2= 0.97, 0.98, 0.99. The results suggest that adsorption was predominantly chemically controlled, involving chemisorption as the rate-limiting step. In contrast, pseudo-first-order and Elovich models yielded lower regression coefficients. Their computed parameters were given in the Table 3. However, kinetic models used for only to study reaction rate, they do not describe the diffusion mechanism of As (III) ions. Therefore, further Weber-Morris model has been investigated to study the As (III) adsorption. The adsorption of As (III) ions involves the following three phases: initial phase (15-45 min) corresponds to rapid movement of As (III) from the bulk solution to the external surface of M-

CPB/LDH composites. Second Phase (60-90 min) is governed by intra-particle diffusion, where As (III) ions diffuse into the internal pores of M-CPB/LDH composites and here, adsorption rate is higher due to availability numerous of active sites. Finally, equilibrium phase (up to 120 min) is characterized by a gradual approach to equilibrium, primarily controlled by pore diffusion and sorption rate stabilizes as available sites are already occupied [63-64]. As stated by Weber-Morris that if q_t vs. $t^{0.5}$ plot cross the origin than intra particle diffusion is the major rate-limiting step. However, as shown in Fig. 11(a), As (III) sorption did not pass through the origin, indicating that sorption does not involve single-step mechanism. Rather, the findings indicate that adsorption is dictated by film diffusion and intra particle diffusion which occur together.

3.2.5. Temperature and thermodynamics

To explore the thermodynamics study, temperature of As (III) ions solution were varied from 30 °C to 60 °C with CPB, M-LDH and M-CPB/LDH composites. Fig. 11(b) present the temperature study and it was found that with a rise in temperature, As (III) adsorption was increased. Maximum adsorption efficiencies of 88.95 %, 92.18 %, and 96.76 % were achieved for CPB, M-LDH, and M-CPB/LDH composites, respectively, at 65 °C under optimum conditions. This trend indicates a positive relationship between temperature and adsorption capacity, verifying the endothermic adsorption. The improvement in adsorption capacity can be credited to the superior binding ability of As (III) ions at the active adsorbent sites under elevated

temperatures. Moreover, at higher temperature activation energy boosted the As (III) ion mobility and the pore texture of the adsorbent for easier permeability and adsorption of As (III) ions. Following equations compute the value of ΔH° and ΔS° [65-66]:

$$\Delta G^\circ = \Delta H^\circ - T\Delta S^\circ \quad (12)$$

$$\ln K_D = \frac{\Delta S^\circ}{R} - \frac{\Delta H^\circ}{RT} \quad (13)$$

Distribution ratio (K_D) can be calculated as:

$$K_D = \frac{q_e}{C_e} \quad (14)$$

Where, K_D and q_e (mg/g) indicates the distribution coefficient and sorption capacity of adsorbent, respectively and R gas constant (8.314 J/mol/K). Table 4 summarizes the parameters computed for As (III) ions adsorption using prepared composites. The Gibbs free energy (ΔG°) values were negative, confirming the feasibility and spontaneity of adsorption process (Fig. 11c). Positive enthalpy (ΔH°) values (17.37 KJ/mol, 32.44 KJ/mol and 45.54 KJ/mol using CPB, M-LDH and M-CPB/LDH, respectively) indicates that adsorption process is of endothermic. Additionally, the positive entropy (ΔS°) values of 83.64 J/mol/ K, 91.53 J/mol/ K and 162.03 J/mol/ K were computed using CPB, M-LDH and M-CPB/LDH, respectively specify the solid-liquid interface

exhibit randomness upon sorption of As (III) ions, possibly because of the displacement of water molecules and structural reorganization of adsorbate-adsorbent interactions.

3.2.6. Mechanism of As (III) adsorption

The passible mechanism of As (III) ions adsorption onto M-CPB/LDH nanocomposites has been given in the Fig. 12. The mechanism of action may involve the electrostatic attraction and ligand exchange. The negatively charged arsenate species are initially attracted to the positively charged M-CPB/LDH surface, while surface –OH groups subsequently undergo ligand exchange to form stable inner-sphere M–O–As complexes. This synergistic interaction ensures strong binding of As (III) ions with M-CPB/LDH surface.

3.2.7. Regeneration, reuse and comparison of monolayer adsorption capacity

Desorption and recyclability are critically connected for assessing the real-world applicability of an adsorbent. Hence, CPB, M-LDH and M-CPB/LDH composites were regenerated with acidic eluents. In particular, 0.01 mol/L HCl was utilized as the desorbing agent for As (III) ions removal from loaded composites. For desorption experiments, As (III)-loaded composites added into 100 mL of 0.01 mol/L HCl solution in Erlenmeyer flasks under the optimized reaction conditions. The suspensions were mechanically agitated at 170 rpm for 24 h, and after this, composites were magnetically separated from the solution. Following desorption, equilibrium concentration of As (III)

in solution was analyzed by AAS and clean with distilled water thoroughly upto neutral pH, we obtained and then, reused for seven adsorption-desorption cycles (as mentioned in Section 2.5). Fig. 13 shows the adsorption efficiency of CPB, M-LDH, and M-CPB/LDH composites for seven successive cycles. At the seventh cycle, adsorption efficiency reduced to 78.19 % for CPB, 83.13 % for M-LDH, and 91.45 % for M-CPB/LDH composites. This accounts for a loss of around 8 % in adsorption efficiency for CPB and M-LDH and 5 % for M-CPB/LDH composites. The small decline due to partial desorption of As (III) ions, which causes a steady decline in accessible adsorption sites in subsequent cycles [67]. Interestingly, M-CPB/LDH composites showed great reusability with high adsorption capacity and negligible loss of efficiency, which makes them propitious for practical applications. The computed Q_m value for As (III) metal ions using CPB, M-LDH, and M-CPB/LDH composites were compared with other reported adsorbents. Table 5 illustrates the compare the sorption performance of other adsorbents and our synthesized M-CPB/LDH composites imparted the descent adsorption efficiency over adsorbents reported in the literature. Therefore, M-CPB/LDH composites has been regarded as economical, green and efficient material for elimination of toxic As (III) ions.

Conclusion

In present laboratory scale research work, CPB, M-LDH and M-CPB/LDH composites were explored for the removal of toxic As (III) ions. The microstructure and chemical compositions of samples has been analyzed by

FTIR, XRD, FESEM-EDX elemental mapping, BET, TGA, VSM and XPS. These instrumental techniques confirmed the successful synthesis of targeted composites. The adsorption of As (III) ions onto CPB, M-LDH, and M-CPB/LDH composites was confirmed using FESEM-EDX analysis and elemental mapping, which showed significant As (III) peak in the corresponding spectra. The surface area of M-CPB/LDH composites was found to be higher than that of CPB, correlating with enhanced As (III) ion removal efficiency. The VSM study reveal that maximum saturation magnetization (Ms) of M-LDH and M-CPB/LDH composites were recorded to be 33.59 and 30.87 emu/g, respectively. These values showed that M-CPB/LDH composites is attracted by magnetic field from the aqueous solution. The maximal adsorption of As (III) ions were recorded at 4.0 pH and dominant mechanisms involve surface complexation including outer-sphere complexation and ligand exchange mechanism. The equilibrium sorption of As (III) ions onto CPB, M-LDH and M-CPB/LDH composites have been strongly co-related with Langmuir and pseudo-second-order model with greater values of regression coefficients, suggesting monolayer and chemisorptive adsorption. Desorption of As (III) ions indicates that it can be efficiently removed from the adsorbent surface under acidic conditions, maintaining a high adsorption even after seven cycles. The use of M-CPB/LDH composites as an adsorbent for As (III) ions proved to be highly efficient, emphasizing its potential for practical water purification. Even, while the findings of our laboratory-scale experiments were promising, but testing with

actual waste-water effluents might provide different results. This is because real water effluents are more complex, containing multiple co-existing ions, fluctuating pH, ionic strength, organic matter, and other interfering materials that can affect the performance of the composites being studied. Overall, findings suggest that synthesized M-CPB/LDH composite is an environmentally benign, economic and innovative, offering a promising alternative for As (III) contamination.

Declaration section

Ethical approval

Not applicable.

Consent to participate

Not applicable.

Consent to publish

Not applicable.

Competing interests

The authors declare no competing interests.

Clinical Trial

Not applicable.

Funding

The authors extend their appreciation to the Deanship of Scientific Research at King Khalid University for funding this work through Large Groups Project under grant number (RGP.1/76/45). The authors extend their appreciation to Maharishi Markandeshwar University (Deemed to be University), Mullana, Ambala for providing the laboratory and necessary instrumental support.

Author contribution statement

Arush Sharma: Writing–review & editing, Writing–original draft, Software, Data curation. **Suchi Sharma and Ajay Kumar:** Formal analysis, Visualization. **Nadeem Sharma and Abhishek Thakur:** Investigation. Methodology, Investigation, Data curation. **Anand Somvanshi, Rohit Jasrotia and Deepak Pathania:** Supervision. **Abdulrhman Alsayari and Shadma Wahab:** Resources. **Allah Dekama Jara:** Writing-Review and Editing, Resources.

Data Availability Statement

Data will be made available from the corresponding author on a request.

References

1. Bessaies H, Iftekhar S, Doshi B, Kheriji J, Ncibi MC, Srivastava V, Sillanpää M, Hamrouni B (2020) Synthesis of novel adsorbent by intercalation of biopolymer in LDH for the removal of arsenic from synthetic and natural water. J Environ Sci: 91 246-261.
2. Turk T, Boyraz T, Alp İ (2024) Arsenic removal by layered double hydroxides (LDH): A mini review. Water Pract. Technol: 19(5) 2088-2107.

3. Brahma D, Barman MP, Basak D, Saikia H (2025) Prospects of layered double hydroxide (LDH)-based adsorbents for the remediation of environmental inorganic pollutants from wastewater: a critical review. Environmental Science. Water Res Technol.
4. Adlnasab L, Shekari N, Maghsodi A (2019) Optimization of arsenic removal with Fe_3O_4@ Al_2O_3@ Zn-Fe LDH as a new magnetic nano adsorbent using Box-Behnken design. J Environ Chem Eng: 7(2) 102974.
5. Borges GA, Ferreira GM, Siqueira KP, Dias A, Navarro KO, e Silva SJ, Rodrigues GD, Mageste AB (2020) Adsorption of organic and inorganic arsenic from aqueous solutions using MgAl-LDH with incorporated nitroprusside. J Colloid Interface Sci: 575 194-205.
6. Yadav MK, Gupta AK, Ghosal PS, Mukherjee A (2019) Modeling and analysis of adsorptive removal of arsenite by Mg–Fe–(CO_3) layer double hydroxide with its application in real-life groundwater. J Environ Sci Health: 54(13) 1318-36.
7. Hong J, Zhu Z, Lu H, Qiu Y (2014) Synthesis and arsenic adsorption performances of ferric-based layered double hydroxide with α-alanine intercalation. Chem Eng J: 252 267-74.
8. Li S, Xu H, Wang L, Ji L, Li X, Qu Z, Yan N (2021) Dual-functional sites for selective adsorption of mercury and arsenic ions in [SnS4] 4-/MgFe-LDH from wastewater. J Hazard Mater : 403 123940.
9. Sun, Y., Yu, F., Han, C., Houda, C., Hao, M., & Wang, Q. (2022) Research Progress on Adsorption of Arsenic from Water by Modified Biochar and Its Mechanism: A Review. *Water; 14*(11), 1691.
10. Meng Z, Lv F, Li X, Zhang Q, Chu PK, Komarneni S, Zhang Y (2016) Simultaneous arsenate and alkali removal from alkaline wastewater by in-situ formation of Zn–Al layered double hydroxide. Micropor Mesopor Mat: 227 137-43.
11. Bagherifam S, Komarneni S, Lakzian A, Fotovat A, Khorasani R, Huang W, Ma J, Wang Y (2014) Evaluation of Zn–Al–SO_4 layered double

hydroxide for the removal of arsenite and arsenate from a simulated soil solution: isotherms and kinetics. Appl Clay Sci: 95 119-25.

12. Mandal S, Sahu MK, Patel RK (2013) Adsorption studies of arsenic (III) removal from water by zirconium polyacrylamide hybrid material (ZrPACM-43). Water Resour Ind: 4 51-67.
13. Borges GA, Ferreira GM, Siqueira KP, Dias A, Navarro KO, e Silva SJ, Rodrigues GD, Mageste AB (2020) Adsorption of organic and inorganic arsenic from aqueous solutions using MgAl-LDH with incorporated nitroprusside. J Colloid Interface Sci: 575 194-205.
14. Kasneryk V, Gazenbiller E, Wieland DF, Garamus VM, Serdechnova M, Blawert C, Zheludkevich ML (2025) From Zn-Al LDH to ZIF-8@ Zn-Al LDH conversion coatings on the surface of AA2024 alloy: inside the process and the effect of the transformation on the protective properties. S&I: 105958.
15. Ardau C, Frau F, Lattanzi P (2013) New data on arsenic sorption properties of Zn–Al sulphate layered double hydroxides: Influence of competition with other anions. Appl Clay Sci: 80 1-9.
16. Meng Z, Lv F, Li X, Zhang Q, Chu PK, Komarneni S, Zhang Y (2016) Simultaneous arsenate and alkali removal from alkaline wastewater by in-situ formation of Zn–Al layered double hydroxide. Micropor Mesopor Mat: 227 137-43.
17. Li A, Deng H, Ye C, Jiang Y (2020) Fabrication and characterization of novel ZnAl-layered double hydroxide for the superadsorption of organic contaminants from wastewater. ACS omega: 5(25) 15152-61.
18. Ma X, Li S, Ren H, Zhang Y, Ma Z (2022) Egg white-mediated fabrication of Mg/Al-LDH-hard biochar composite for phosphate adsorption. Molecules: 27(24) 8951.
19. Yang Q, Cui P, Liu C, Fang G, Huang M, Wang Q, Zhou Y, Hou H, Wang Y (2021) In situ stabilization of the adsorbed Co2+ and Ni2+ in

rice straw biochar based on LDH and its reutilization in the activation of peroxymonosulfate. Journal of Hazardous Materials. : 416 126215.

20. Li S, Dong L, Wei Z, Sheng G, Du K, Hu B (2020) Adsorption and mechanistic study of the invasive plant-derived biochar functionalized with CaAl-LDH for Eu (III) in water. J Environ Sci: 96 127-37.
21. Xue L, Gao B, Wan Y, Fang J, Wang S, Li Y, Muñoz-Carpena R, Yang L (2016) High efficiency and selectivity of MgFe-LDH modified wheat-straw biochar in the removal of nitrate from aqueous solutions. J Taiwan Inst Chem Eng: 63 312-7.
22. Nguyen TM, Van HT, Yılmaz M, Hoang TK, Nguyen QT, Vi TM, Nga LT (2022) Removal of Tetracycline from aqueous solution using composite adsorbent of ZnAl layered double hydroxide and bagasse biochar. Environ Techno Innov: 28 102914.
23. Bai Y, Ma R, Jing Z, Wan X, Tong J, Huang W, Liu J (2024) Synthesis of Zn/Al layered double hydroxides magnetic-nanoparticle for removal of humic acid. DESALIN WATER TREAT: 317 100097.
24. Wang Y, Zhang L, Hou H, Xu W, Duan G, He S, Liu K, Jiang S (2021) Recent progress in carbon-based materials for supercapacitor electrodes: a review. J Mater Sci: 56 173-200.
25. Li, N., Zhu, F., Wang, Z., Wu, J., Gao, Y., Li, K., Zhao, C., & Wang, X. (2025) Harnessing corn straw biochar: A breakthrough in eco-friendly Cu(II) wastewater treatment. *Waste Management, 197*, 25–34.
26. Dinh TD, Zhang D, Tuan VN (2020) High iodine adsorption performances under off-gas conditions by bismuth-modified ZnAl-LDH layered double hydroxide. RSC Adv: 10(24) 14360-7.
27. Wang J, Zhang T, Li M, Yang Y, Lu P, Ning P, Wang Q (2018) Arsenic removal from water/wastewater using layered double hydroxide derived adsorbents, a critical review. RSC Adv: 8(40) 22694-709.
28. Yang, H., Wang, X., Wang, J., Liu, H., Jin, H., Zhang, J., Li, G., Tang, Y., & Ye, C. (2025) High-value utilization of agricultural waste: A

study on the catalytic performance and deactivation characteristics of iron-nickel supported biochar-based catalysts in the catalytic cracking of toluene. *Energy, 323*, 135806.

29. Adaileh, A., Ragab, A. H., Taher, M. A., Gumaah, N. F., Ahmad, I. A., Selim, H., & Mubarak, M. F. (2025) Development of Cu-ZnO ZrO_2 based polyacrylonitrile polymer composites for removing pharmaceutical pollutants and heavy metals from wastewater. *Scientific Reports, 15*(1), 22250.

30. Lawal SY, Batagarawa SM, Musa A (2024) Effect of Citrus sinensis peel-derived biochar on the concentrations of heavy metals in soil irrigated with municipal wastewater. JJBRPAC: 1(1) 18-22.

31. Shen Z, Zhang J, Hou D, Tsang DC, Ok YS, Alessi DS (2019) Synthesis of MgO-coated corncob biochar and its application in lead stabilization in a soil washing residue. Environ Int: 122 357-62.

32. G Fouad H, S Amin A, S Ahmed I, A Ali A (2022) Zinc-aluminium layered double hydroxides: Fabrication, study and adsorption application for removal organic dye from aqueous media. Benha J Appl Sci : 7(4) 53-61.

33. Manjula Rani K, Palanisamy PN (2018) Synthesis and characterization of mesoporous, nanostructured zinc aluminium carbonate layered double hydroxides (ZAC-LDHs) and its calcined product (CZA-LDH). J Inorg Organomet Polym Mater : 28 1127-35.

34. Pasieczna-Patkowska, S., & Madej, J. (2018) Comparison of photoacoustic, diffuse reflectance, attenuated total reflectance and transmission infrared spectroscopy for the study of biochars. *Polish Journal of Chemical Technology, 20*(4).

35. Dehkhoda AM, Ellis N, Gyenge E (2014) Electrosorption on activated biochar: effect of thermo-chemical activation treatment on the electric double layer capacitance. J Appl Electrochem: 44 141-57.

36. D Tang Y, Zhang X, Li X, Bai J, Yang C, Zhang Y, Xu Z, Jin X, Jiang Y (2023) Facile synthesis of magnetic ZnAl layered double

hydroxides and efficient adsorption of malachite green and Congo red. Sep Purif Technol : 322 124305.

37. Pathania D, Kumar A, Saini AK, Saini R, Mittal D, Sharma A (2024) Biochar supported Ag/Cu-ZrO2 nano-hetero assembly for enhanced adsorption of heavy metal ions and biomedical applications. Nanotechnol Environ Eng: 2 189-206.

38. Thakur M, Kumar A, Sharma A, Pathania D (2024) Synthesis of Potato-Starch Based Bio-nanocomposite for the Removal of Trifluralin Under Visible Light Illumination. CHEM AFR: 4 1981-93.

39. Sharma A, Thakur M, Kumar A, Pathania D, Sharma A (2024) Fabrication of xyloglucan-based zirconium (IV) selenophosphate nanostructure for removal of deflazacort and antimicrobial applications. SCENV : 7 100131.

40. Din SU, Azeez A, Haq S, Hafeez M, Imran M, Hussain S, Alarfaji SS (2021) Investigation on cadmium ions removal from water by a nanomagnetite based biochar derived from Eleocharis dulcis. J Inorg Organomet Polym Mater: 31 415-25.

41. Majamo SL, Amibo TA, Bedru TK (2023) Synthesis and application of biomass-derived magnetic biochar catalyst for simultaneous esterification and trans-esterification of waste cooking oil into biodiesel: modeling and optimization. Mater Renew Sustain Energy: 2 147-58.

42. Barnabas MJ, Parambadath S, Nagappan S, Ha CS (2019) Sulfamerazine Schiff-base complex intercalated layered double hydroxide: synthesis, characterization, and antimicrobial activity. Heliyon: 5 (4).

43. Fayad, E., Binjawhar, D. N., Elsaid, F. G., Taha, A., & Mubarak, M. F. (2025) Innovative CuZnCr-BTC framework for enhanced Congo red dye removal in sustainable wastewater treatment. *Journal of Cluster Science, 36*(4), 125.

44. Kumari P, Pal B, Das RK (2021) Superior adsorptive removal of eco-toxic drug diclofenac sodium by Zn–Al LDH· xBi2O3 layer double hydroxide composites. Appl Clay Sci : 208 106119 .

45. Wu K, Xu J, Jiang Y, Jiang Y, Yurekli Y, Yue X, Dai Y, Zhang T, Yang D, Qiu F (2025) ZnAl-LDH/wood-based antifouling membranes for high-flux and efficient oil/water separation. J Hazard Mater: 27 137739.

46. Rao M Xia, H Xu, Y Jiang, G Zhang, Q Yuan, Y and Zhang L (2024) Study on ultrasonic assisted intensive leaching of germanium from germanium concentrate using HCl/NaOCl. Hydrometallurgy, 230, 106385.

47. Zhang H, Deng Y, Yang J, Yin J, Wang J, Xiao H, Wang L, Zhang C, Wang W (2023) Selective transformation and removal of As (III) by constructed Fe− N bonds: The generation of singlet oxygen from the photoexcitation of MnPc leads to abundant ZnFe− LDH interface OH radical. Sci Total Environ: 890:164314.

48. Rahman S, Navarathna CM, Das NK, Alchouron J, Reneau P, Stokes S, Thirumalai RV, Perez F, Hassan EB, Mohan D, Pittman Jr CU (2021) High capacity aqueous phosphate reclamation using Fe/Mg-layered double hydroxide (LDH) dispersed on biochar. J Colloid Interface Sci : 597:182-95.

49. Zhu Y, Laipan M, Zhu R, Xu T, Liu J, Zhu J, Xi Y, Zhu G, He H (2017) Enhanced photocatalytic activity of Zn/Ti-LDH via hybridizing with C60 . MOL CATAL: 427 54-61.

50. Li X, Yu Z, Shao L, Zeng H, Liu Y, Feng X (2020) A novel strategy to construct a visible-light-driven Z-scheme (ZnAl-LDH with active phase/g-C3N4) heterojunction catalyst via polydopamine bridge (a similar" bridge" structure) J Hazard Mater : 386 121650.

51. Zou J, Wang Z, Guo W, Guo B, Yu Y, Wu L (2020) Photocatalytic selective oxidation of benzyl alcohol over ZnTi-LDH: The effect of surface OH groups. Appl Catal B : 260 118185.

52. Li S, Dong L, Wei Z, Sheng G, Du K, Hu B (2020) Adsorption and mechanistic study of the invasive plant-derived biochar functionalized with CaAl-LDH for Eu (III) in water. J Environ Sci : 96 127-37.

53. Smith M, Scudiero L, Espinal J, McEwen JS, Garcia-Perez M (2016) Improving the deconvolution and interpretation of XPS spectra from chars by ab initio calculations. Carbon : 110 155-71.

54. Peighambardoust, S.J., Abdollahian Aghbolagh, S., Foroutan, R., & Peighambardoust, N.S. (2025) Decontamination of crystal violet using nanocomposite adsorbent based on pine cone biochar modified with $CoFe_2O_4$/Mn-Fe LDH. *Scientific Reports, 15*(1), 15067.

55. Li, N., Zhu, F., Wang, Z., Wu, J., Gao, Y., Li, K., Zhao, C., & Wang, X. (2025) Harnessing corn straw biochar: A breakthrough in eco-friendly Cu(II) wastewater treatment. *Waste Management, 197*, 25–34.

56. Wang S, Gao B, Li Y, Zimmerman AR, Cao X (2016) Sorption of arsenic onto Ni/Fe layered double hydroxide (LDH)-biochar composites. RSC Adv: 6(22) 17792-9.

57. Lee SH, Choi H, Kim KW (2018) Removal of As (V) and Sb (V) in aqueous solution by Mg/Al-layered double hydroxide-incorporated polyethersulfone polymer beads (PES-LDH). Environ Geochem Health: 40 2119-29.

58. Kumari S, Sharma A, Dhiman P, Thakur M, Aloui Z, Selvaraj M, Kumar A (2025) Strategic synthesis of biowaste-derived magnetic hydrochar for adsorption and photocatalytic removal of Chlorpyrifos herbicides from simulated wastewater. MSEB : 314 118009 .

59. Gao C, Yu XY, Luo T, Jia Y, Sun B, Liu JH, Huang XJ (2014) Millimeter-sized Mg–Al-LDH nanoflake impregnated magnetic alginate beads (LDH-n-MABs): a novel bio-based sorbent for the removal of fluoride in water. J Mater Chem A: 2(7) 2119-28.

60. Pu, S., Ma, H., Deng, D., Xue, S., Zhu, R., Zhou, Y., & Xiong, X. (2018) Isolation, identification, and characterization of an *Aspergillus*

niger bioflocculant-producing strain using potato starch wastewater as nutrilite and its application. *PLoS ONE, 13*(1), e0190236.

61. Sharma A, Siddiqi ZM, Pathania D (2017) Adsorption of polyaromatic pollutants from water system using carbon/ZnFe2O4 nanocomposite: equilibrium, kinetic and thermodynamic mechanism. J Mol Liq : 240 361-71
62. Dharmapriya TN, Li D, Chung YC, Huang PJ (2021) Green synthesis of reusable adsorbents for the removal of heavy metal ions. ACS Omega: 6(45) 30478-87.
63. Sharma A, Sharma G, Naushad M, Ghfar AA, Pathania D (2018) Remediation of anionic dye from aqueous system using bio-adsorbent prepared by microwave activation. Environ Technol : 39(7) 917-30.
64. Kumar A, Pathania D, Gupta N, Raj P, Sharma A (2020) Photo-degradation of noxious pollutants from water system using Cornulaca monacantha stem supported ZnFe2O4 magnetic bio-nanocomposite. Sustain Chem and Pharm:1;18:100290.
65. Zubair M, Daud M, McKay G, Shehzad F, Al-Harthi MA (2017) Recent progress in layered double hydroxides (LDH)-containing hybrids as adsorbents for water remediation. Appl Clay Sci : 143 279-92.
66. Das S, Dash SK, Parida KM (2018) Kinetics, isotherm, and thermodynamic study for ultrafast adsorption of azo dye by an efficient sorbent: ternary Mg/(Al+ Fe) layered double hydroxides. ACS Omega: 3(3) 2532-45.
67. Su, L., Wu, S., Fu, G., Zhu, W., Zhang, X., & Liang, B. (2024). Creep characterisation and microstructural analysis of municipal solid waste incineration fly ash geopolymer backfill. *Scientific Reports, 14*(1), 29828.Çiftçi TD, Henden E (2015) Nickel/nickel boride nanoparticles coated resin: A novel adsorbent for arsenic (III) and arsenic (V) removal. J Powder Technol : 269 470-80.

List of Figures

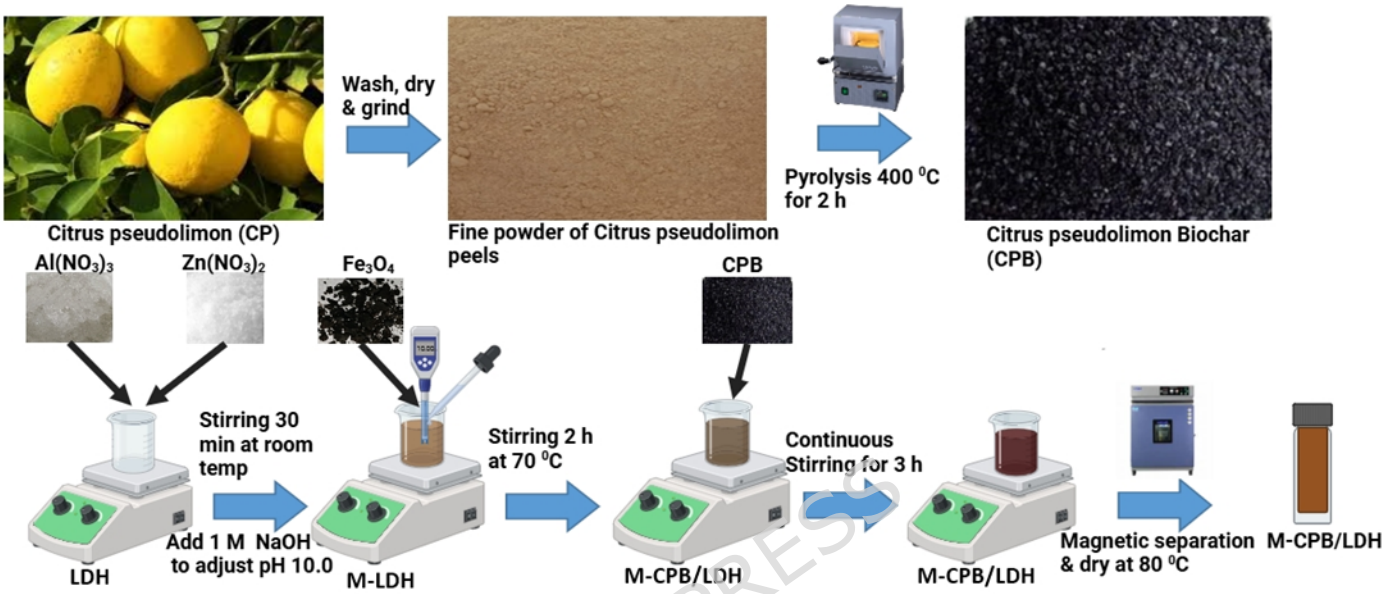

Fig. 1: Schematic illustration of M-CPB/Zn+Al (LDH) synthesis.

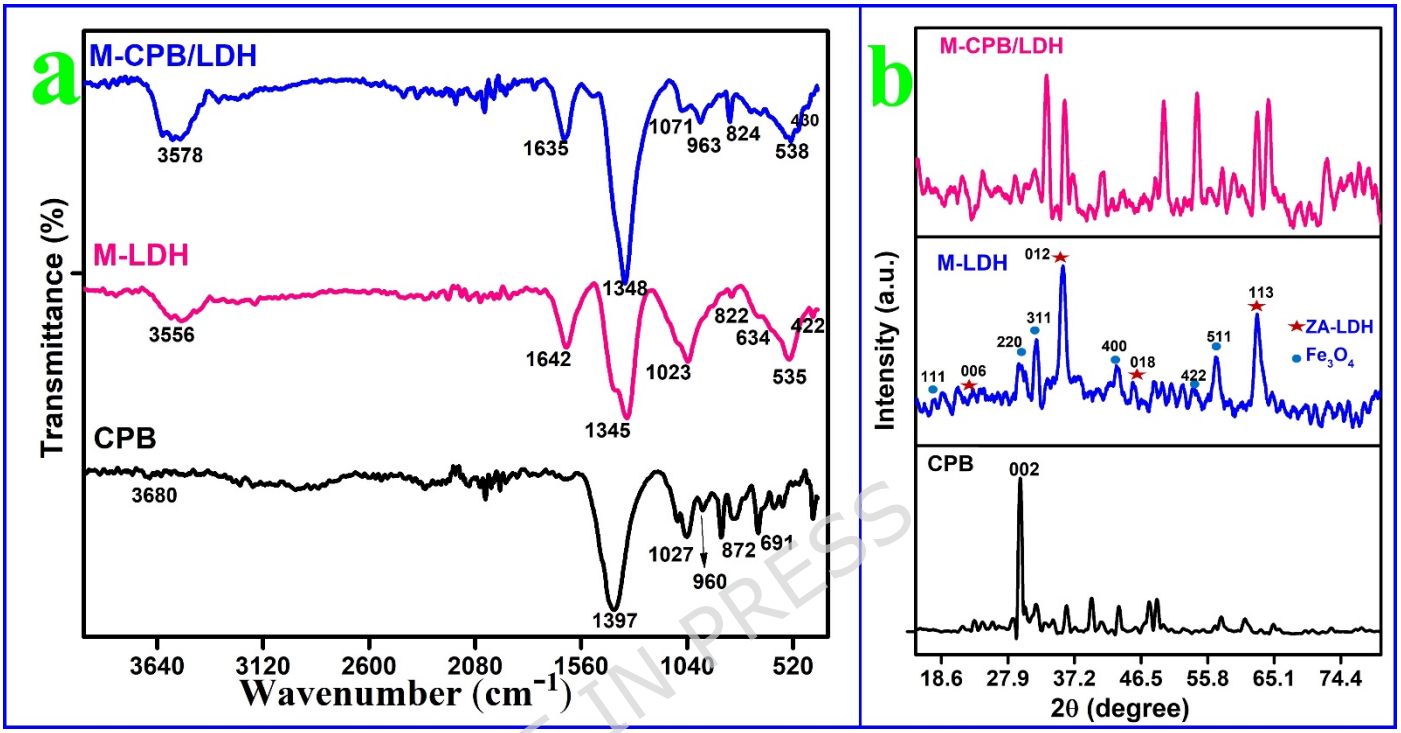

Fig. 2. (a-b) FTIR and XRD spectra of CPB, M-LDH and M-CPB/LDH composites.

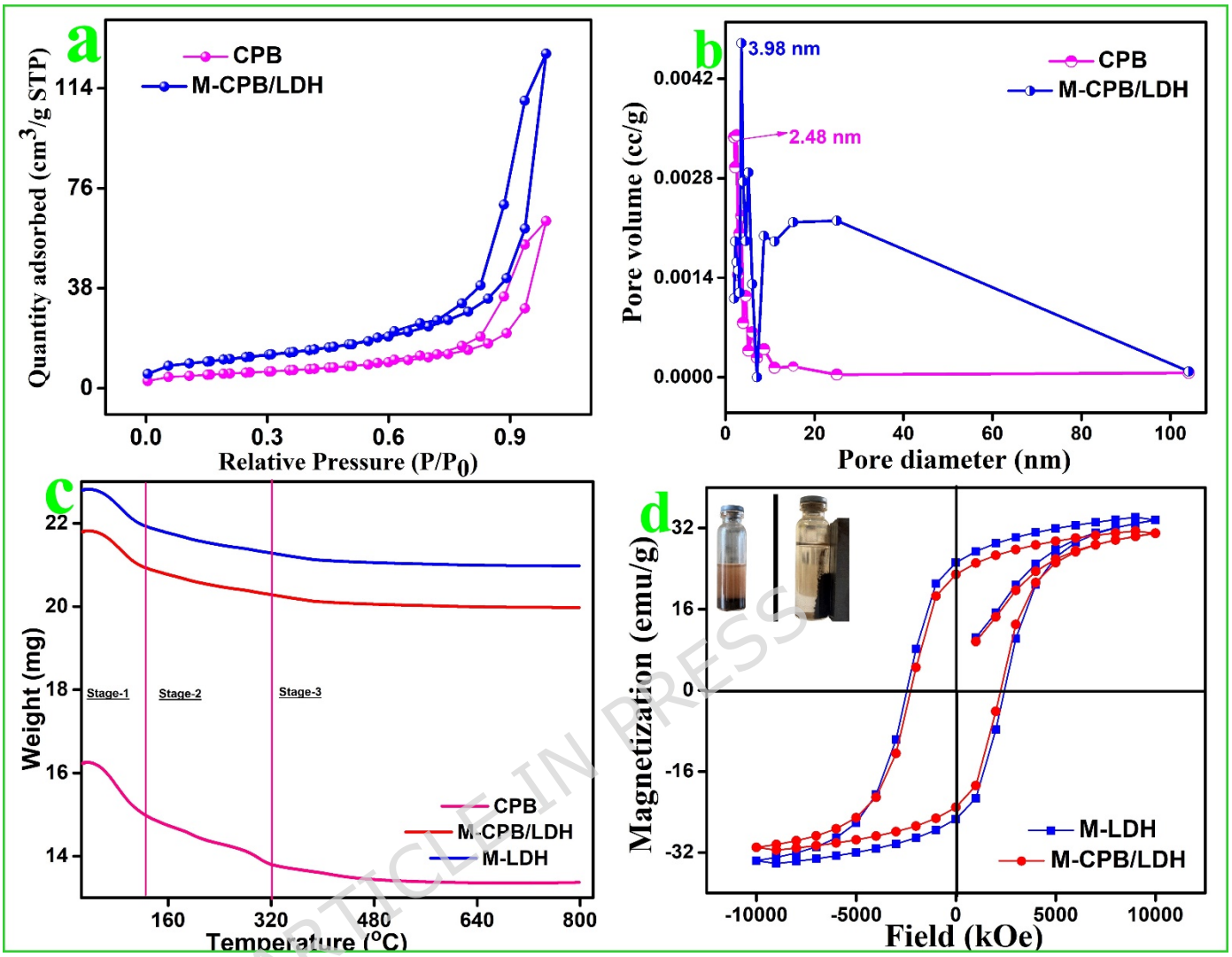

Fig. 3. (a) BET surface area, (b) Pore size distribution (PSD) plot and (c) TGA curve, (d) Magnetization hysteresis loop (inset: Seperation efficiency of M-CPB/LDH composites)

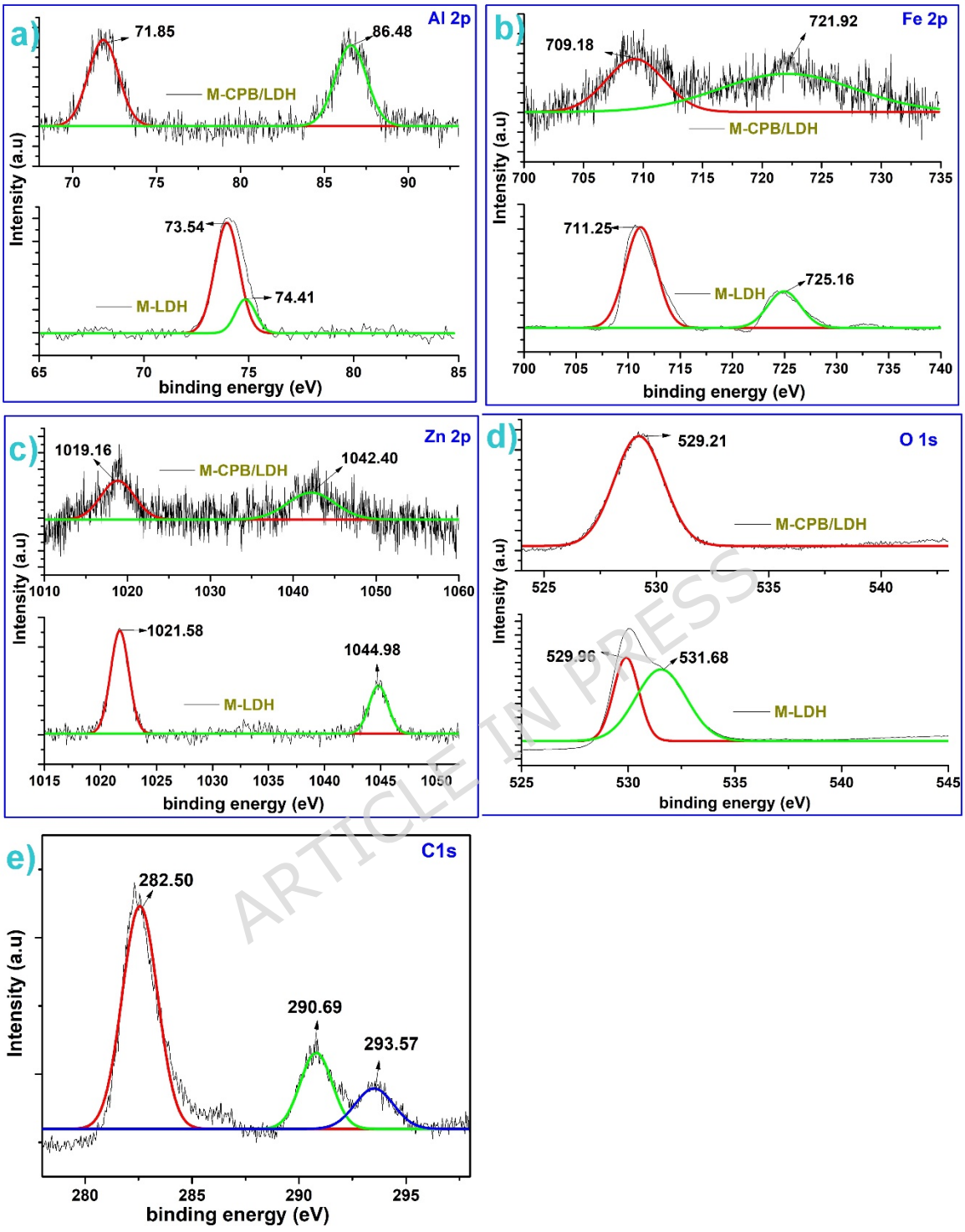

Fig. 4. Deconvoluted XPS spectrum for M-LDH & M-CPB/LDH a) Al 2p, b) Fe 2p, c) Zn 2p, d) O 1s and e) C 1s.

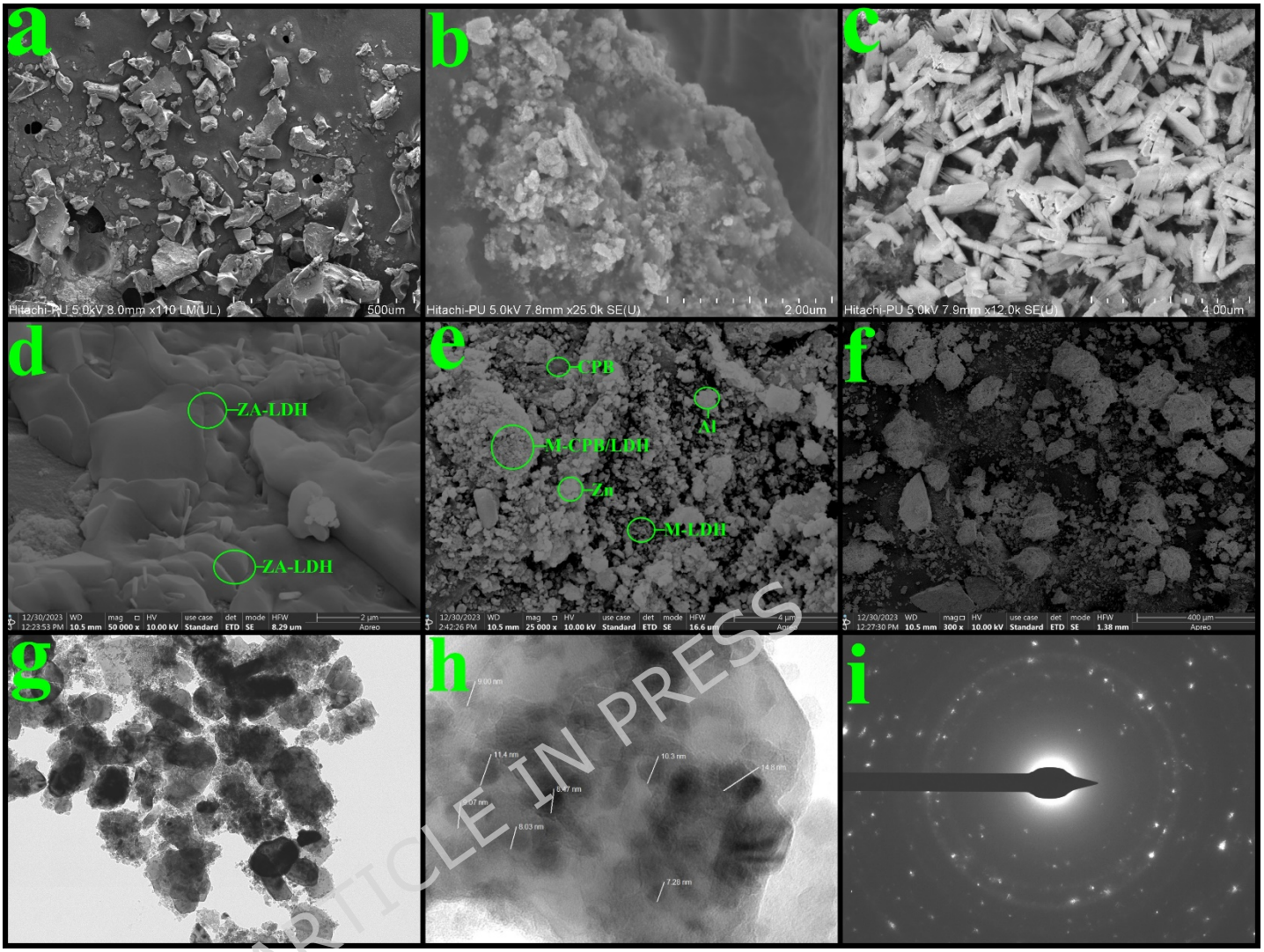

Fig. 5. (a-c) FESEM images of CPB at different magnifications, (d) ZA-LDH, (e-f) FESEM images of M-CPB/LDH, (g-h) HRTEM images of M-CPB/LDH and (i) SAED pattern.

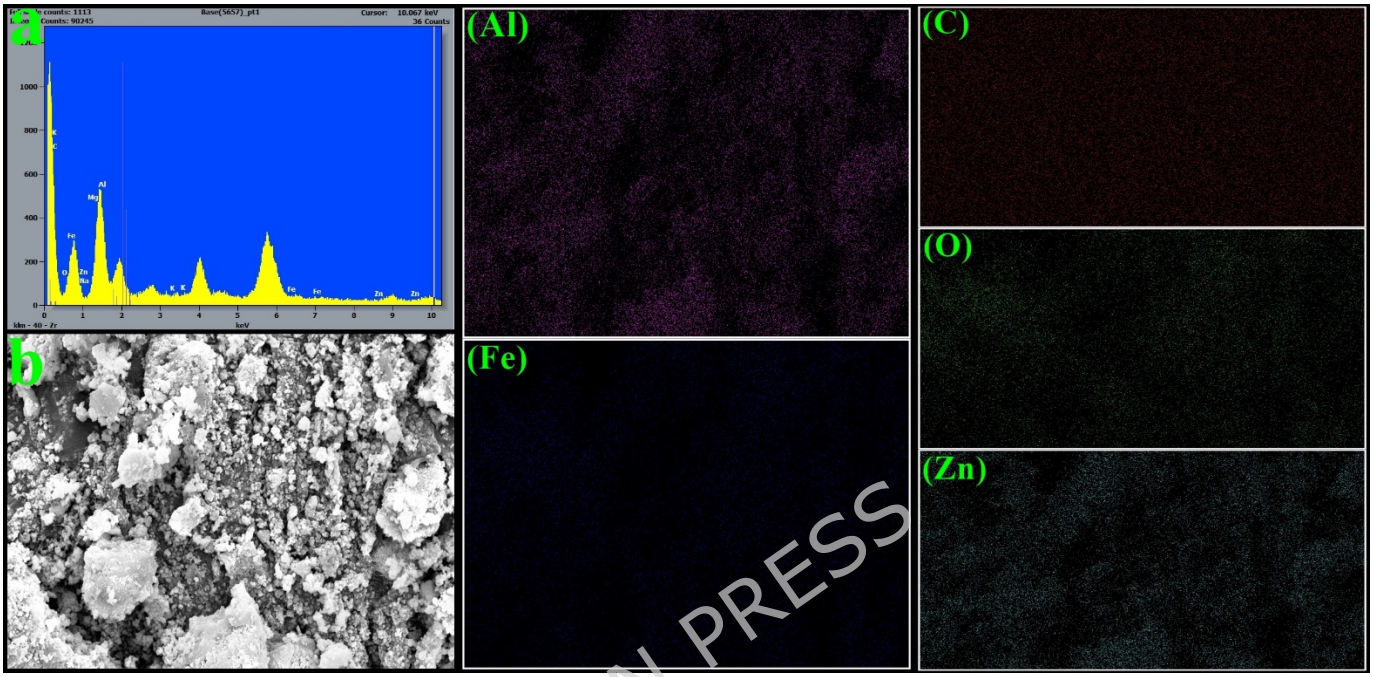

Fig. 6. (a-b) EDS spectrum and FESEM image of M-CPB/LDH with elemental mapping showing Al, Fe, C, O and Zn elements.

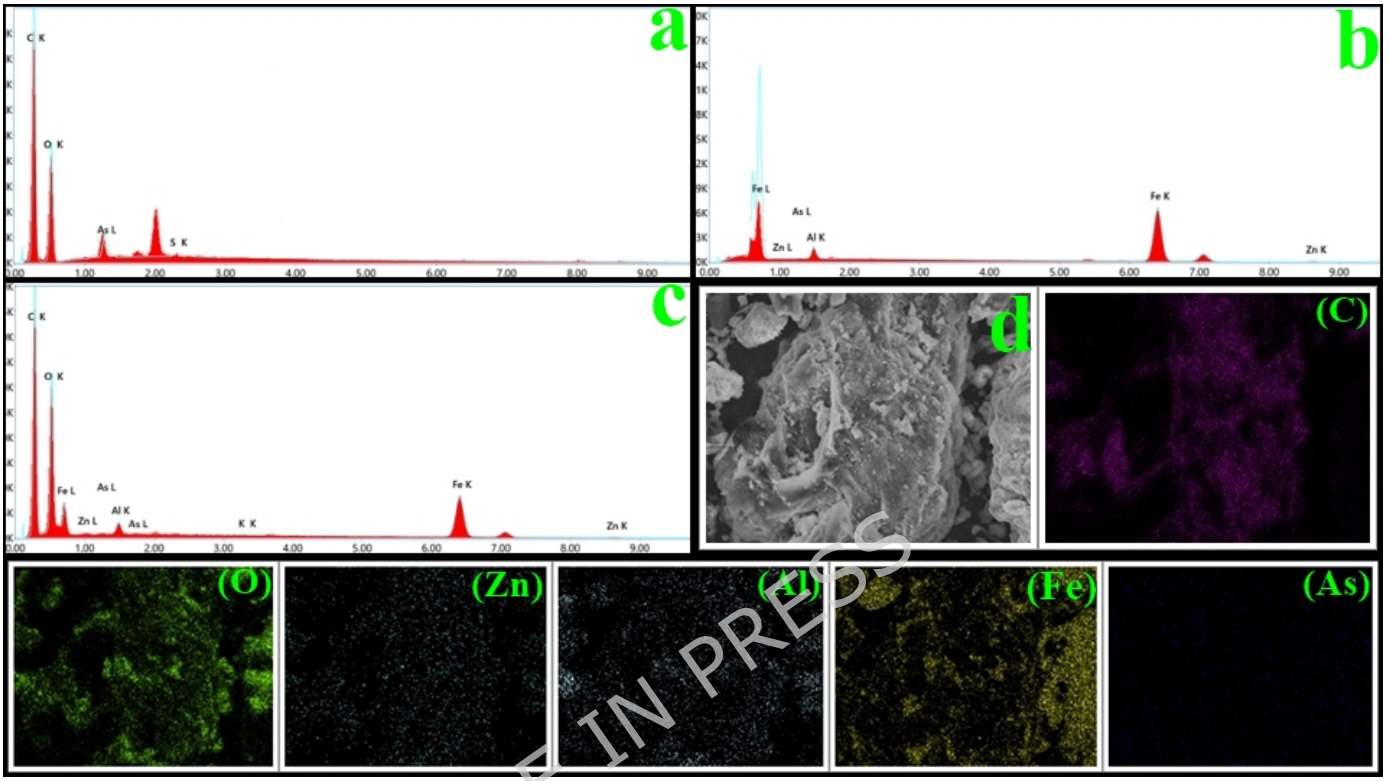

Fig. 7. (a-c) EDS spectra of CPB, M-LDH and M-CPB/LDH loaded As (III) ions, (d) FESEM image of M-CPB/LDH composites after As (III) adsorption followed by individual elemental mapping.

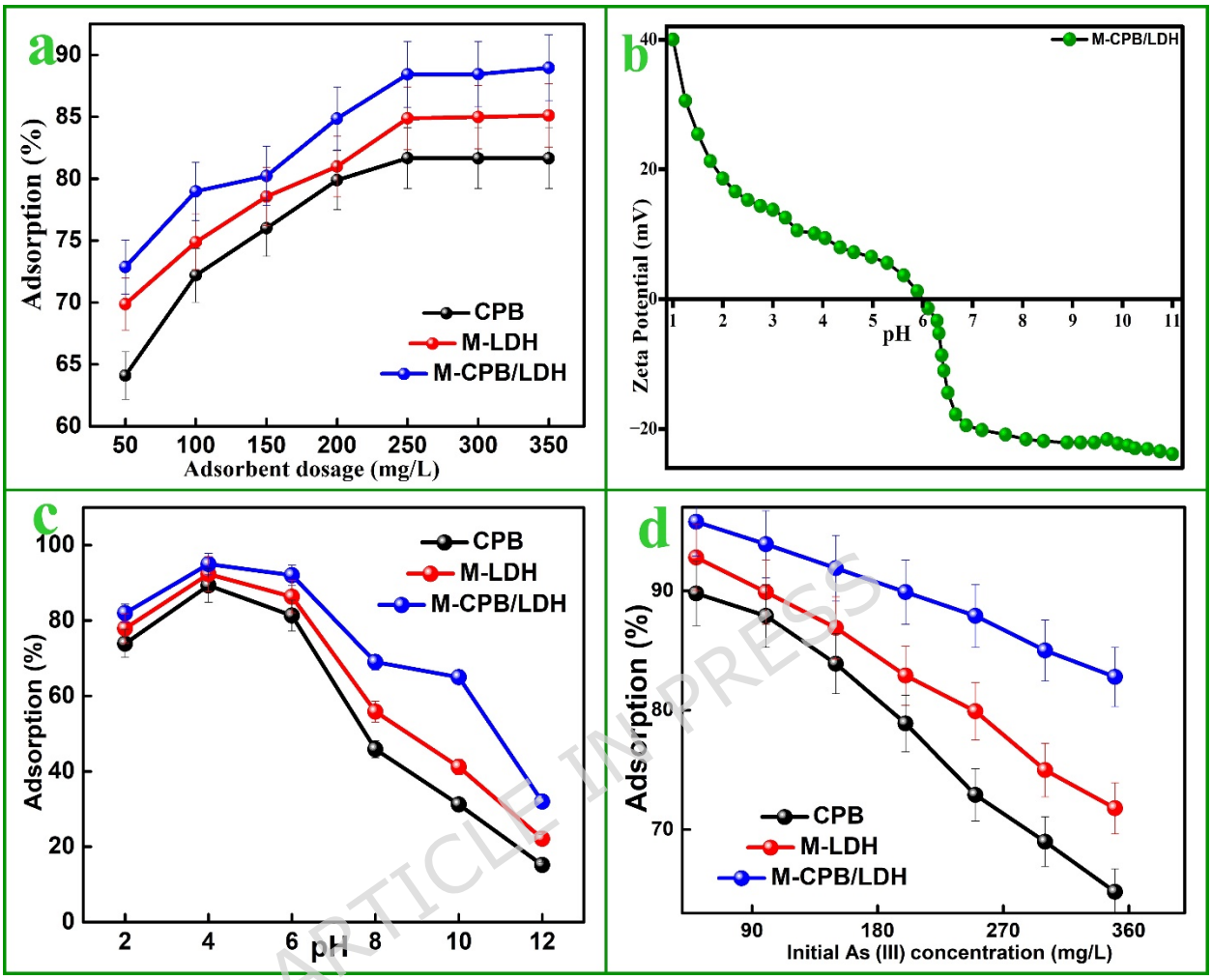

Fig. 8. (a) Effect of adsorbent dosage, (b) zeta potential, (c) pH effect, (d) initial As (III) concentration [Optimized condition: Adsorbent dosage 0.250 g, Initial As (III) concentrations 50 mg L^{-1}, contact time 90 min, pH 4.0 and temperature 60 °C].

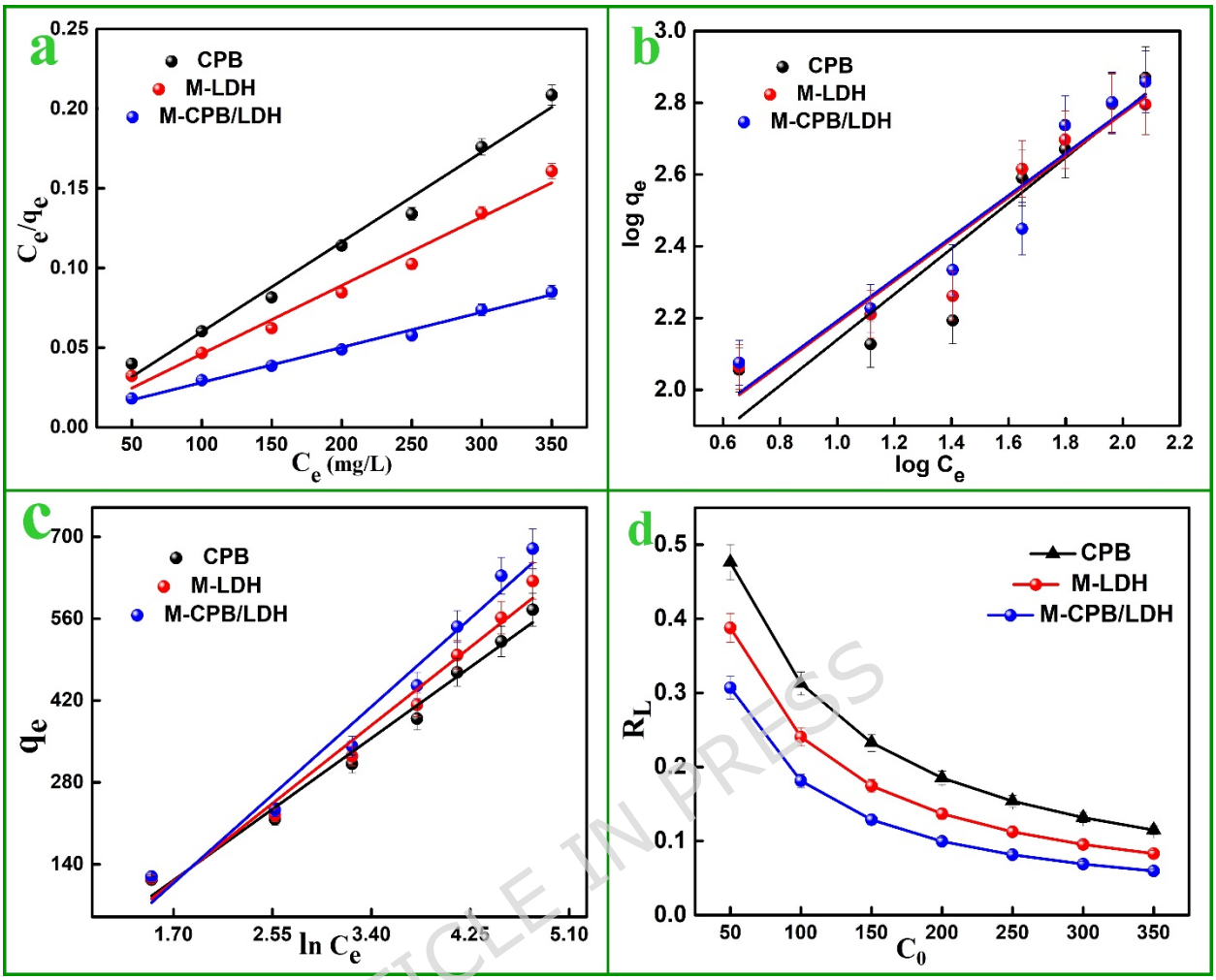

Fig. 9. (a-c) Langmuir, Freundlich and Temkin isotherm (d) R_L Plot

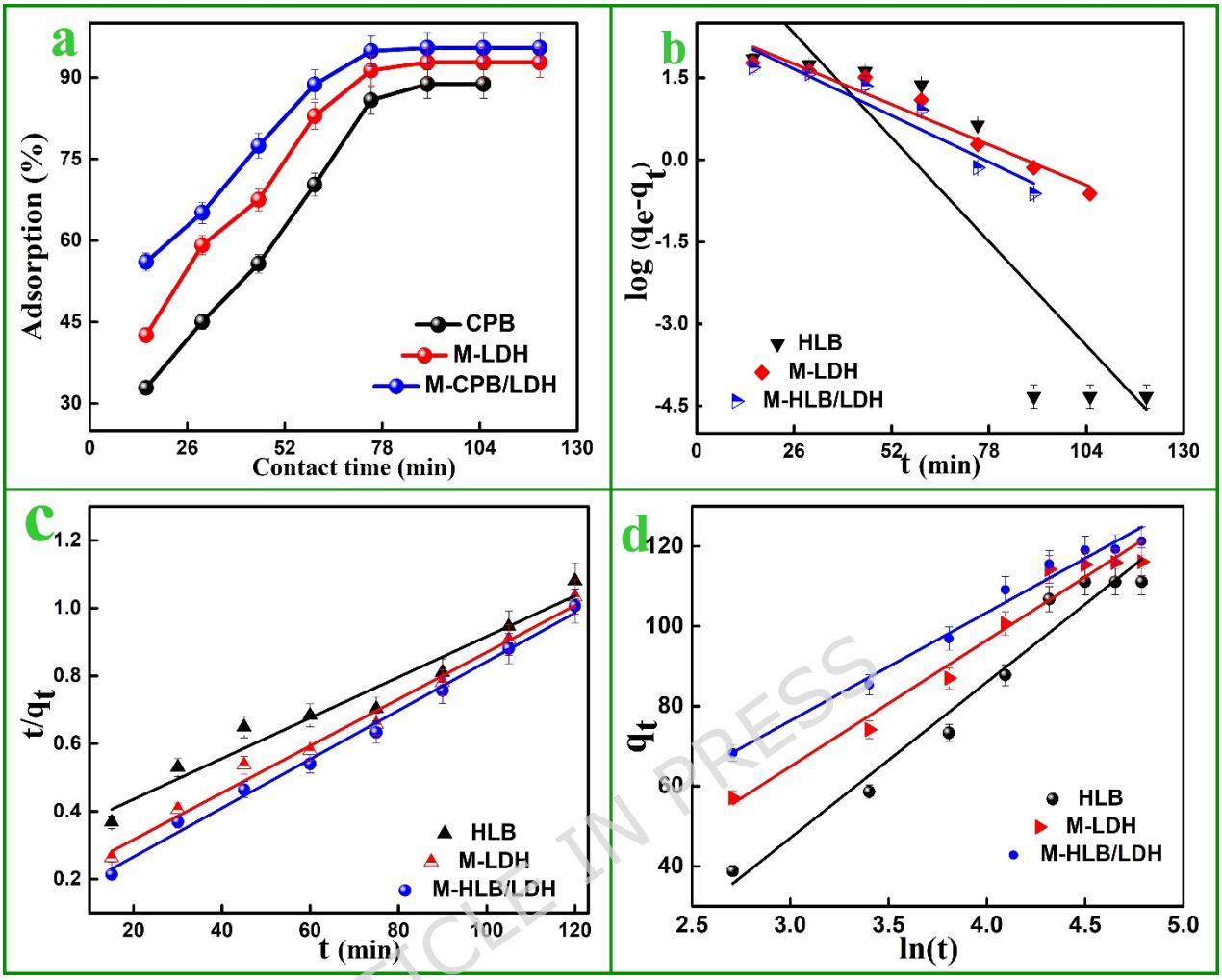

Fig. 10. (a) Effect of contact time, (b) pseudo-first-order, (c) pseudo-first-order, (d) Elovich model

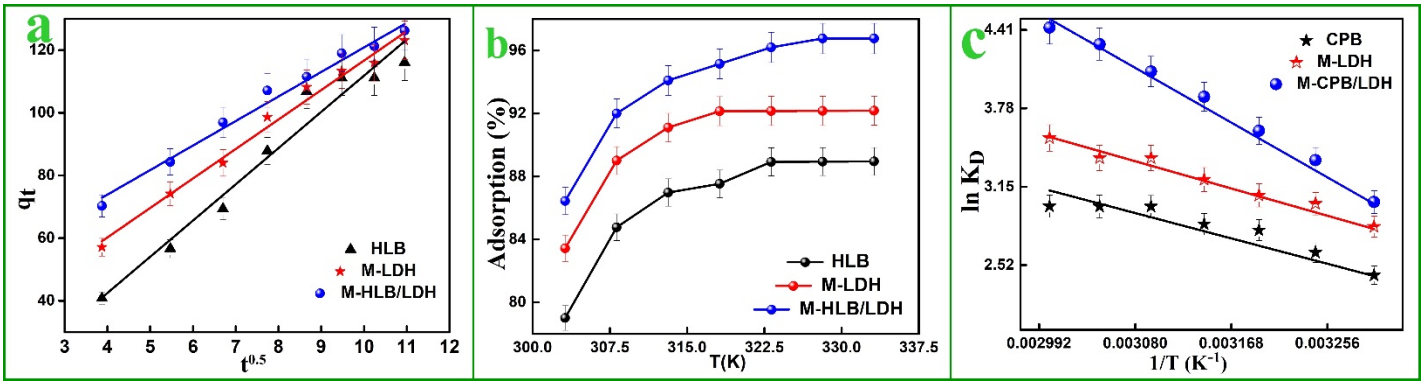

Fig. 11. (a) Intra-particle diffusion model, (b) temperature effect and (c) Vent Hoff plot.

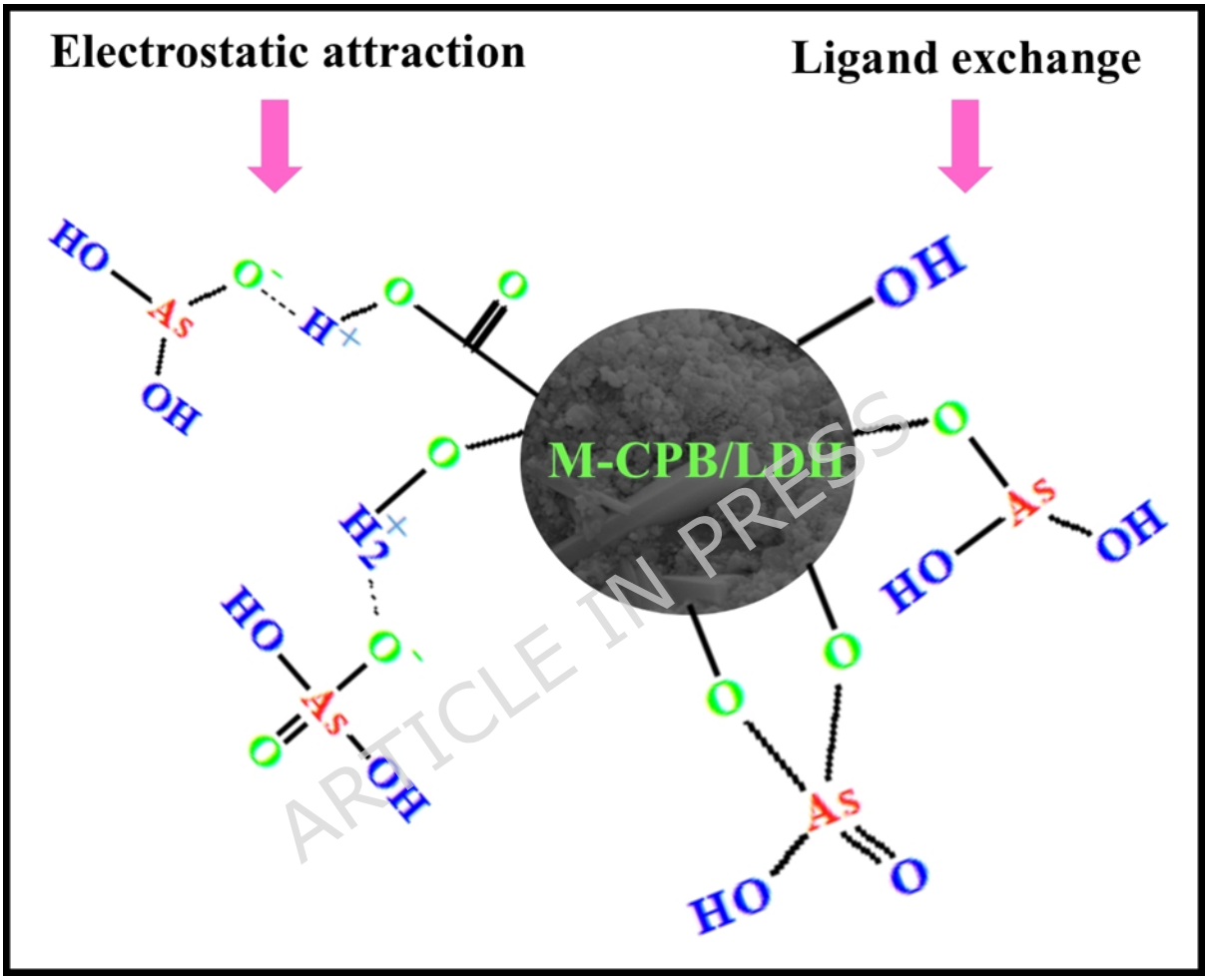

Fig. 12. Adsorption mechanism of As (III) ions using M-CPB/LDH nanocomposites.

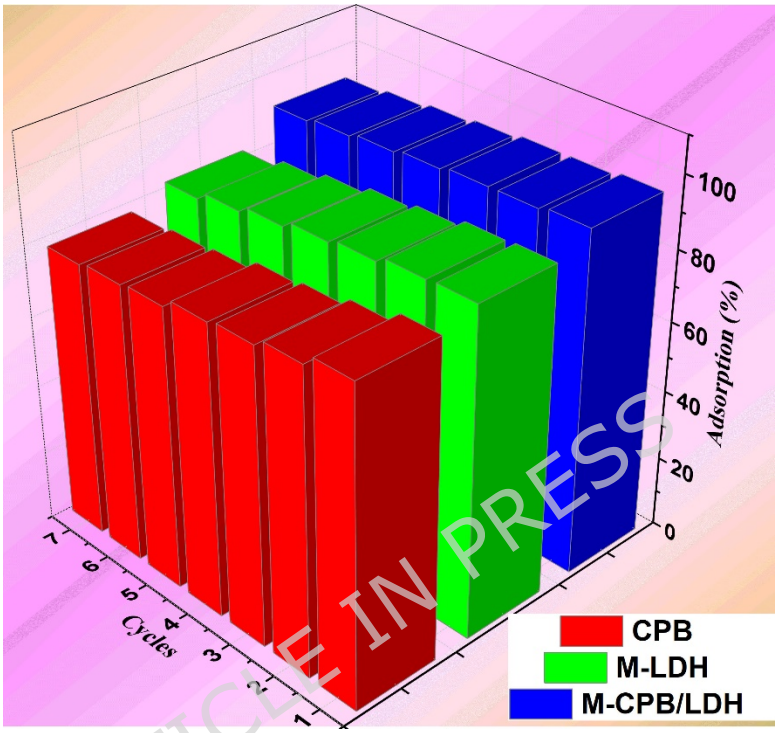

Fig. 13. Recycle study of CPB, M-LDH and M-CPB/LDH nanocomposite for As (III) adsorption from aqueous phase.

List of Tables

Table 1: Magnetic parameters of synthesized samples:

Samples	Magnetic coercivity (Hc-KQe)	Retentivity (Mr- emu g^{-1})	Saturation magnetization (Ms- emu g^{-1})
M-CPB/LDH	23010	21.78	30.87
M-LDH	2577	25.26	33.59

Isotherm and parameters	CPB	M-LDH	M-CPB/LDH
Langmuir			
Q_m (mg g^{-1})	575.10	624.34	721.34
k_L (L mg^{-1})	0.022	0.0316	0.0452
R_L	0.476-0.114	0.387-0.082	0.306-0.059
R^2	0.97	0.98	0.99
Freundlich			
K_F (L g^{-1})	34.38	53.99	67.10
n	1.80	2.34	2.76
R^2	0.87	0.91	0.91
Temkin			
k_T (mg g^{-1} h^{-2})	2.48	3.73	5.89
B ((g mg^{-1} h^{-2})	142.79	157.06.	184.02
R^2	0.98	0.97	0.97

Table 2. Adsorption models for As (III) sorption onto synthesized samples.

Table 3. Kinetic study of As (III) sorption onto synthesized samples.

Adsorbents	CPB	M-LDH	M-CPB/LDH
Pseduo-first-order			
q_e (mg g^{-1})	12.09	15.10	14.69
K_1 (h^{-1})	0.028	0.073	0.064
R^2	0.76	0.93	0.90
Pseduo-second-order			
q_e (mg g^{-1})	138.74	144.17	164.74
K_2 (g mg^{-1} min^{-1})	0.00011	0.00026	0.00010
R^2	0.97	0.98	0.99
Elovich			
α (mg g^{-1} h^{-2})	49.77	59.48	78.58
β (g mg^{-1})	0.256	0.0316	0.0305
R^2	0.95	0.96	0.97
Weber-Morris			
C (mg g^{-1})	3.74	31.18	52.59
k_{id} (mg g^{-1} $h^{0.5}$)	15.06	10.51	3.92
R^2	0.95	0.98	0.98

Table 4. Thermodynamic study of As (III) adsorption onto synthesized samples.

Temperature (k)	ΔG° (KJ/mol)		
	CPB	M-LDH	M-CPB/LDH
303.15	-25.33	-27.71	-49.07
308.15	-25.75	-28.17	-49.88
314.15	-26.25	-28.69	-50.85
318.15	-26.59	-29.08	-51.50
323.15	-27.01	-29.54	-52.31
328.15	-27.44	-30.00	-53.12
333.15	-27.84	-30.46	-53.93
338.15	-28.26	-30.91	-54.74
ΔH° (KJ/mol)	17.37	32.44	45.54
ΔS° (J/mol/ K)	83.64	91.53	162.03

Table 5: Comparative maximum adsorption capacity (Q_m) of As (III) ion onto various types of adsorbents.

Serial no.	Adsorbents	Q_m (mg g^{-1})	Reference	Serial no.	Adsorbents	Q_m (mg g^{-1})	Reference
1	Nickel/nickel boride	23.4	[58]	9	Fe–Cu binary oxide	122.3	[65]
2	Mn–Fe–CO3	112.5	[59]	10	Hollow Fe–Ce alkoxides	266	[66]
3	CZA	30.15	[60]	11	Fe_2O_3	60.65	[67]

					– diatomite		
4	Mg–Al–MoS4 LDH	99	[61]	12	Fe_2O_3 – macroporous silica	320	[68]
5	CCA	10.91	[60]	13	FeO x–CNS-13	416	[69]
6	Mg–Fe–Cl	286.9	[62]	14	CPB	575.10	Present study
7	a-alanine (MgeFe-Ala-LDH	49.8	[63]	15	M-LDH	624.34	Present study
8	Fe_3O_4 nanoparticles (12 nm)	160	[64]	16	M-CPB/LDH	721.34	Present study